Coastal Engineering 168 (2021) 103947

Contents lists available at ScienceDirect

Coastal Engineering

journal homepage: www.elsevier.com/locate/coastaleng

Wave attenuation by suspended canopies with cultivated kelp (*Saccharina latissima*)

Longhuan Zhu [a,*], Jiarui Lei [b], Kimberly Huguenard [a], David W. Fredriksson [c]

[a] Department of Civil and Environmental Engineering, University of Maine, Orono, ME, 04469, USA
[b] Department of Civil and Environmental Engineering, Massachusetts Institute of Technology, Cambridge, MA, 02139, USA
[c] Department of Naval Architecture and Ocean Engineering, U.S. Naval Academy, Annapolis, MD, 21402, USA

ARTICLE INFO

Keywords:
Wave attenuation
Kelp
Saccharina latissima
Bulk drag coefficient
Effective blade length
Suspended canopies

ABSTRACT

Many kelp aquaculture farms consist of moored arrays of long horizontal lines that grow kelp near the water surface. Most kelp farms are deployed in the same direction of wave propagation. However, with numerous longlines of densely grown kelp, these farms may have the potential to attenuate waves if installed perpendicular to the direction of wave propagation. In this application, the kelp farm may serve as a form of nature-based coastal protection. To assess this potential, a set of 1:10 scale physical model experiments were conducted to measure the wave attenuation of a suspended kelp model. The model was scaled based on the morphological and mechanical properties of the cultivated *Saccharina latissima* (sugar kelp) from Saco Bay, Maine, USA. Experimental results demonstrated that suspended blades have asymmetric oscillatory motions with more bending in the opposite direction of wave propagation. Due to severe asymmetric blade motion in large waves, the suspended blade could roll over the attached line following the wave orbital motion. The results also showed that suspended kelp farms in the designed configuration with 20 longlines of 1-m-long blades and 100 blades/m have the potential attenuating wave energy by up to 33.7% under the experimental wave conditions. Based on the experimental data, empirical formulas were developed for the bulk drag coefficient (C_{DB}) and effective blade length (l_e) of suspended kelp canopies for wave attenuation. To predict wave attenuation under a wider range of conditions and to identify the key parameters affecting wave attenuation, a numerical model was developed that could resolve blade motion. The benefits of resolving blade motion were to improve the model accuracy and reduce the number of experiments needed for obtaining C_{DB} or l_e, which is required in the conventional wave attenuation models based on the rigid blade assumption. The results indicate that (i) the wave energy dissipation ratio (EDR defined as the ratio of the dissipated wave energy to the incident wave energy) of suspended kelp farms decreases with increased water depth, (ii) EDR is not sensitive to wave height, (iii) EDR first increases and then decreases with wavelength, and (iv) EDR increases with blade size, kelp vertical position, plant density, and the number of longlines. Therefore, the technique to improve the wave attenuation capacity of suspended kelp farms for nature-based coastal defense is to install the kelp farms in shallower water, expand the farm size by adding more longlines, locate the kelp in a higher position of the water column, grow the kelp more densely, and choose the kelp species with more rigid, wider, and longer blades/biomass.

1. Introduction

Kelp is considered one of many types of brown macroalgae seaweeds that contribute to coastal ecosystems by providing food, shelter, and enhanced oxygen habitats for fish and marine animals. Kelp also provides services such as recycling inorganic nutrients, preventing eutrophication, reducing carbon dioxide concentration, and potentially mitigating ocean acidification (Duarte et al., 2017; Stévant et al., 2017; Xiao et al., 2017; Campbell et al., 2019; Bricknell et al., 2020). Furthermore, the existence of kelp can physically influence the environmental hydrodynamics. For example, *Macrocystis pyrifera* (giant kelp) forests can significantly reduce currents (Jackson, 1997; Gaylord et al., 2007; Rosman et al., 2007) and internal wave amplitudes (Jackson, 1984; Rosman et al., 2007) off west coast of California, USA. However, no significant (surface) wave attenuation was observed over *M. pyrifera* forests by Elwany et al. (1995), which is likely due to the compliant

* Corresponding author.
E-mail address: longhuan.zhu@maine.edu (L. Zhu).

https://doi.org/10.1016/j.coastaleng.2021.103947
Received 8 September 2020; Received in revised form 19 April 2021; Accepted 20 June 2021
Available online 21 June 2021

nature of the kelp, the sparse canopy density (~ 0.1 plants/m^2) and the limited canopy height related to the water depths (typical averages of 10 m). Similar results are also observed for highly flexible *Nereocystis luetkeana* bull kelp,Gaylord et al. (2003) and deeply submerged *Ecklonia radiata* (< 10% of the water column, Morris et al., 2019). However, *Laminaria hyperborea* (tangle) with 25 plants/m^2 in shallow water (5 m) have been observed to reduce wave energy by 70%–85% over a distance of 258 m (Mork, 1996).

Unlike wild kelp that grows on the seafloor, kelp aquaculture farms that float may also have the potential to dissipate wave energy, especially since surface wave energy is concentrated near the surface. Furthermore, many kelp aquaculture farms are densely seeded to maximize economic output. With densely cultivated kelp, suspended farms may provide more favorable wave attenuation than naturally occurring kelp beds containing a sparse plant density.

Wave attenuation theories for submerged canopies including wild kelp beds have been developed by Dalrymple et al. (1984) and Kobayashi et al. (1993) by assuming rigid kelp and vegetation subject to monochromatic wave action. These wave attenuation models were then extended for flexible vegetation (Asano et al., 1992; Méndez et al., 1999; Mullarney and Henderson, 2010; Riffe et al., 2011; Luhar et al., 2017; Lei and Nepf, 2019b; Zhu et al., 2020a), random waves (Mendez and Losada, 2004; Chen and Zhao, 2012; Jacobsen et al., 2019; Zhu et al., 2020a), and combined waves and currents (Hu et al., 2014; Losada et al., 2016; Chen et al., 2018; Yin et al., 2020). To analyze the effects of blade motion on wave attenuation, Asano et al. (1992) and Méndez et al. (1999) simplified the blade motion as an oscillator with one degree of freedom by assuming blade deflection is linearly distributed along the blade length and averaging the deflection along the length. To obtain the depth dependent blade deflection, Rosman et al. (2013) discretized the blade into segments and solved the force balance equations for each segments by assuming negligible bending momentum and shear stresses between adjacent segments. To obtain the analytical solutions for blade motion considering bending momentum and shear stresses, Mullarney and Henderson (2010), Riffe et al. (2011), and Henderson (2019) modeled the blade as a continuous cantilever beam by using Euler–Bernoulli techniques and ignoring the blade inertia and inertia forces.Recently, Zhu et al. (2020a, 2021) extended the analytical solutions for blade motion by incorporating the inertia forces for both chromatic wave and random waves. These analytical solutions are achieved by assuming a small deflection to linearize the blade curvature. To consider the nonlinear blade curvature (geometric nonlinearity) in large blade motion, numerical methods are often used (e.g., Zeller et al., 2014; Luhar and Nepf, 2016; Chen and Zou, 2019; Zhu et al., 2020b). Recently, Zhu et al. (2020b) used a cable model to capture the asymmetric "whip-like" blade motion and proposed mechanisms for the asymmetric blade motion in symmetric waves.

The wave attenuation theories developed by Dalrymple et al. (1984) and Kobayashi et al. (1993) were then extended to floating and suspended canopies by Plew et al. (2005) and Zhu and Zou (2017), respectively. Zhu and Zou (2017) showed that the suspended and floating canopies can reduce more wave energy than submerged canopies in the same conditions because wave orbital velocities decrease toward the bottom, especially for shorter waves. However, these approaches assumed a rigid canopy component without motion, which may overestimate the wave attenuation. Recently, Zhu et al. (2020a) extended the wave attenuation methods to be frequency dependent for random waves and incorporated the motion of the flexible canopy component. Compared to nearshore submerged aquatic vegetation (SAV), suspended aquaculture structures are less affected by water level changes since suspended aquaculture structures float near the water surface (Zhu et al., 2020a). In one case study, Zhu et al. (2020a) demonstrated that the implementation of aquaculture structures offshore can extend the wave attenuation capacity of SAV-based living shorelines over wider ranges of wave frequency and water level. With numerical techniques, such as the SWASH (Simulating WAves till SHore, Zijlema et al., 2011) model, Chen et al. (2019) investigated the wave-driven circulation cell induced by suspended canopies and found that the vertical position of the canopy also has significant effects on the wave-driven current in the canopy. Although these studies have provided important insight into the wave attenuation potential of suspended aquaculture farms, experimental research to quantify the performance of suspended kelp aquaculture structures is still needed.

Research to examine the hydrodynamic characteristics of kelp blades in steady flow was conducted by Buck and Buchholz (2005). In their study, the drag characteristics of both a single and an aggregate of *Saccharina latissima* (sugar kelp) blades were investigated with tow tests in still water. The results showed sheltering interactions among the blades so that the drag force of an aggregate of kelp blades cannot be estimated by simply superimposing the drag of individual blades. Vettori and Nikora (2019) investigated the turbulent flow interaction with single blades of *S. latissima* in an open-channel flume and showed enhanced turbulence in blade wakes. At low current speeds, the flapping motion of kelp blades of *S. latissima*, *M. pyrifera*, and *N. luetkeana* can significantly enhance the nutrient flux to the blade surface (Huang et al., 2011). Using polyethylene to model *S. latissima*, Vettori and Nikora (2018) found that the model kelp blades increase the turbulence intensity and reduce the mean longitudinal velocity. By comparing the hydrodynamic performance of *S. latissima* with the performance of the model blades, Vettori et al. (2020) showed that the model blades replicated many aspects of *S. latissima* blade dynamics, although the drag force and reconfiguration were underestimated. To avoid the dynamic similarity issues, Fredriksson et al. (2020) conducted full-scale model experiments to understand the hydrodynamics of an aggregate of model *S. latissima* blades in steady flow. Fredriksson et al. (2020) showed a threshold for reconfiguration as the tow speed at which the horizontal component of tangential drag was equal or exceeded the horizontal component of the normal drag. To build upon this work, it is important to examine the dynamics of suspended kelp blades in waves and the value of suspended kelp aquaculture structures for wave attenuation in a laboratory environment. Appropriate parameters from these experiments are essential for modeling wave attenuation with canopy models.

The objective of this study is to quantify the wave attenuation capacity of suspended kelp canopies with a scaled physical model in a set of laboratory experiments. To predict wave attenuation under a wider range of conditions, a simple numerical model was developed based on the blade dynamic model in Zhu et al. (2020b). This model was also used to perform dynamic similarity analysis in preparation for the model tests. The physical model kelp material was chosen from the measured morphological and mechanical properties of cultivated *S. latissima* from Saco Bay, Maine in the USA considering dynamic similarity. The motions of both a single and an aggregate of blades were recorded to analyze the blade dynamics with focus on the mechanisms for observed roll-up and roll-over of suspended blades. The horizontal forces on unsheltered single blades and sheltered blades were measured to examine the differences. The wave height evolution along the suspended canopy was also measured to investigate wave attenuation performance. With the experimental results, bulk drag coefficient and effective blade length estimates for the suspended canopy were developed. The numerical model was compared with the datasets and then used to investigate the potential of using suspended kelp aquaculture structures as nature-based coastal protection.

2. Theory

2.1. Blade dynamics and dynamical similarity

The dynamics of kelp blades in waves can be described using the cable model in Zhu et al. (2020b) by representing the structure as a cantilever beam discretized as blade segments (ds). The velocity

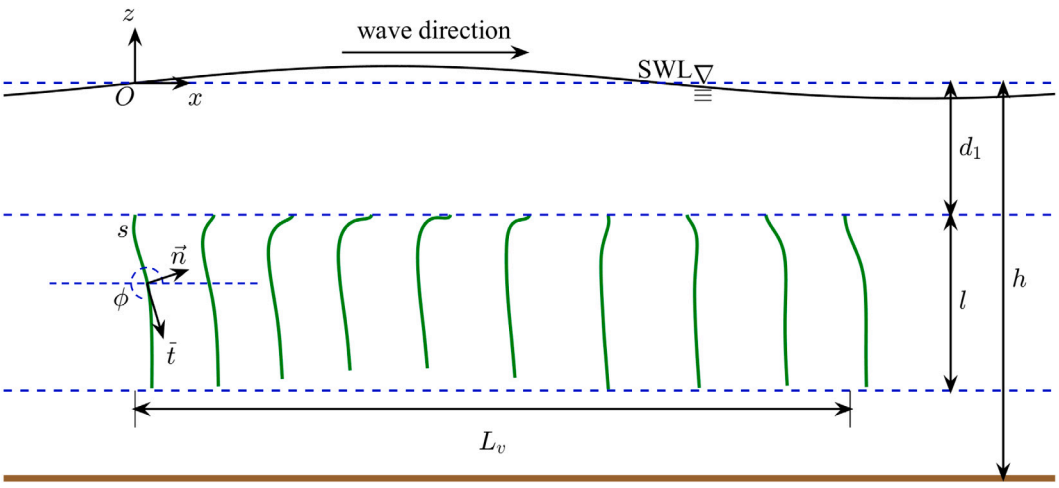

Fig. 1. Sketch for the coordinate systems. The global Cartesian reference frame is (x, z) with $x = 0$ at the leading edge of the canopy and $z = 0$ at the still water level (SWL). A local Lagrangian coordinate system at a distance of s along the blade length (l) is $(\vec{t}, \vec{n})$ with the angle of ϕ between the horizontal line and the blade tangential direction ($\vec{t}$). The suspended blade is fixed at the upper end with distance of d_1 below the SWL. The canopy length is L_v. The water depth is h.

components of the blade segment are defined using a local Lagrangian coordinate system $(\vec{t}, \vec{n})$ along the blade length with $\vec{t}$ representing the blade-tangential direction and $\vec{n}$ as the blade-normal direction (Fig. 1). The velocity components in the blade-tangential direction (u) and normal direction (w) are a function of the distance (s) along the blade length (l) from the fixed end with time (t). The wave velocity field (U, W) is defined using global Cartesian coordinates (x, z), where the horizontal coordinate x is positive in the direction of wave propagation with $x = 0$ at the leading edge of the kelp canopy and the vertical coordinate z is positive upward with $z = 0$ at the still water level (SWL). The angle of the tangential direction ($\vec{t}$) relative to the horizontal direction (x) is ϕ. Thus, the points in the Lagrangian coordinate system $(\vec{t}, \vec{n})$ can be obtained by rotating the global Cartesian coordinates (x, z) counterclockwise by ϕ. In the procedure, a set of normalized variables were applied to the governing equations in Zhu et al. (2020b) and described as,

$$\hat{s} = \frac{s}{l},\ \hat{t} = t\omega,\ \hat{u} = \frac{u}{l\omega},\ \hat{w} = \frac{w}{l\omega},\ \hat{T} = \frac{Tl^2}{EI},\ \hat{U} = \frac{U}{U_m},\ \text{and}\ \hat{W} = \frac{W}{U_m}, \quad (1)$$

where T is the effective tension of the blade, E is the bending elastic modulus, $I = bd^3/12$ is the second moment of the cross-section area of the blade with b the blade width and d the blade thickness, $\omega = 2\pi/T_w$ is the wave angular frequency with T_w the wave period, and U_m is the magnitude of the horizontal wave orbital velocity. Therefore, the dimensionless governing equations for the blade motion are given by

$$\begin{aligned}&\frac{\partial\phi}{\partial\hat{s}}\frac{\partial^2\phi}{\partial\hat{s}^2} + \frac{\partial\hat{T}}{\partial\hat{s}} + B\sin\phi\\ &+\frac{1}{2}C_f 2(1+\delta)Ca\,|-L\hat{u} + \hat{U}\cos\phi + \hat{W}\sin\phi\,|\,(-L\hat{u} + \hat{U}\cos\phi + \hat{W}\sin\phi)\\ &+2\pi\frac{Ca\delta}{KC}\left[-\rho' L\left(\frac{\partial\hat{u}}{\partial\hat{t}} - \hat{w}\frac{\partial\phi}{\partial\hat{t}}\right) + \frac{\partial\hat{U}}{\partial\hat{t}}\cos\phi + \frac{\partial\hat{W}}{\partial\hat{t}}\sin\phi\right] = 0,\end{aligned} \quad (2)$$

$$\begin{aligned}&-\frac{\partial^3\phi}{\partial\hat{s}^3} + \hat{T}\frac{\partial\phi}{\partial\hat{s}} + B\cos\phi\\ &+\frac{1}{2}C_{di}Ca\,|-L\hat{w} - \hat{U}\sin\phi + \hat{W}\cos\phi\,|\,(-L\hat{w} - \hat{U}\sin\phi + \hat{W}\cos\phi)\\ &+C_m 2\pi\frac{Ca\delta}{KC}\left[-L\frac{\partial\hat{w}}{\partial\hat{t}} + \frac{\partial}{\partial\hat{t}}\left(-\hat{U}\sin\phi + \hat{W}\cos\phi\right)\right]\\ &+2\pi\frac{Ca\delta}{KC}\left[-\rho' L\left(\frac{\partial\hat{w}}{\partial\hat{t}} + \hat{u}\frac{\partial\phi}{\partial\hat{t}}\right) - \frac{\partial\hat{U}}{\partial\hat{t}}\sin\phi + \frac{\partial\hat{W}}{\partial\hat{t}}\cos\phi\right] = 0,\end{aligned} \quad (3)$$

$$\frac{\partial\hat{u}}{\partial\hat{s}} + \hat{w}\frac{\partial\phi}{\partial\hat{s}} - \frac{1}{12}\delta^2 S^2\frac{\partial\hat{T}}{\partial\hat{t}} = 0, \quad (4)$$

and

$$\frac{\partial\hat{w}}{\partial\hat{s}} - \hat{u}\frac{\partial\phi}{\partial\hat{s}} + \frac{\partial\phi}{\partial\hat{t}} = 0. \quad (5)$$

The dimensionless parameters governing the blade dynamics include the aspect ratio,

$$\delta = d/b, \quad (6)$$

the slenderness,

$$S = b/l, \quad (7)$$

the length ratio,

$$L = l/A_w, \quad (8)$$

the Keulegan–Carpenter number,

$$KC = U_m T_w/b, \quad (9)$$

the density ratio,

$$\rho' = \rho_v/\rho, \quad (10)$$

the buoyant parameter,

$$B = (\rho - \rho_v)gbdl^3/EI = (1-\rho')Ca/F_r^2, \quad (11)$$

and the Cauchy number,

$$Ca = \rho b U_m^2 l^3/EI, \quad (12)$$

where ρ_v is the blade mass density, ρ is the water density, g is the gravitational acceleration, $A_w = U_m/\omega$ is the wave orbital excursion, and $F_r = U_m/\sqrt{gb}$ is the Froude number. In (2), the friction coefficient is (Abdelrhman, 2007; Zeller et al., 2014)

$$C_f = 0.074Re^{-1/5} \quad (13)$$

with the Reynolds number $Re = U_m b/\nu$ and ν the fluid kinematic viscosity. In (3), the drag coefficient is

$$C_{di} = \max(10KC^{-1/3}, 1.95) \quad (14)$$

and the added mass coefficient is

$$C_m = \min(C_{m1}, C_{m2}) \quad (15)$$

with $C_{m1} = \begin{cases} 1 + 0.35KC^{2/3}, & KC < 20 \\ 1 + 0.15KC^{2/3}, & KC \geq 20 \end{cases}$ and $C_{m2} = 1 + (KC - 18)^2/49$ (Luhar, 2012; Luhar and Nepf, 2016). The formulas for C_{di} and C_m are obtained from the experiments by Keulegan and Carpenter (1958) and Sarpkaya and O'Keefe (1996) for rigid plates in oscillatory flow with KC from 1.7 to 118.2. It is noted that the drag coefficient C_{di} is for an individual blade in oscillatory flow and hereinafter referred

to as "individual drag coefficient" to distinguish from the "bulk drag coefficient" defined in Section 2.2.

The dynamic similarity for the blade motion requires the same dimensionless parameters in (6) to (12) for the model and the full-scale prototype. The aspect ratio (δ), slenderness (S), and length ratio (L) represent the geometrical property and the KC number represent the inertia property of fluid. The similarity for δ, S, L, and KC can be satisfied by Froude similarity criteria (including geometrical similarity). The density ratio ρ', buoyant parameter B, and Cauchy number Ca represent the blade material properties. However, they are not independent as $B = (1-\rho')Ca/F_r^2$ (11). Therefore, two of the following parameters: ρ', B, and Ca are the required criteria to select the material to fabricate the model blades. In a similar approach, Fryer et al. (2015) used ρ' and Ca as the similarity criteria to fabricate the model kelp blade for *Macrocystis* with a silicone-based polymer.

In this study, the blade is fixed and suspended at the upper end ($s = 0$) with tangential direction downward such that $\phi = 3\pi/2$ for the initial static state (Fig. 1). Thus, the boundary conditions are set as $\hat{u} = 0$, $\hat{w} = 0$, and $\phi = 3\pi/2$ at the fixed end with $\hat{s} = 0$, as well as $\hat{T} = 0$, $\partial\phi/\partial\hat{s} = 0$, and $\partial^2\phi/\partial\hat{s}^2 = 0$ at the free end with $\hat{s} = 1$. The relationships between s and (x, z) are

$$x = \int_0^s \cos\phi ds \tag{16}$$

and

$$z = -d_1 + \int_0^s \sin\phi ds, \tag{17}$$

where d_1 is the distance from the upper fixed end of the blade to SWL (Fig. 1). Eqs. (16) and (17) are required to calculate the blade posture and convert the flow velocity from global Cartesian coordinates to local Lagrangian coordinates. Solving the blade dynamical equations (2) to (5) with boundary conditions yields the blade velocity (u, w), effective tension (T), and direction angle (ϕ). The shear force along the blade can be obtained by

$$Q = EI\frac{\partial^2\phi}{\partial s^2}. \tag{18}$$

Details of numerically solving the nonlinear partial differential equations are referred to Zhu et al. (2020b).

2.2. Wave attenuation

For linear waves, the wave orbital velocities are expressed as (Dean and Dalrymple, 1991)

$$U = \frac{H}{2}\omega\frac{\cosh k(h+z)}{\sinh kh}\cos(kx-\omega t) \tag{19}$$

and

$$W = \frac{H}{2}\omega\frac{\sinh k(h+z)}{\sinh kh}\sin(kx-\omega t), \tag{20}$$

where H is the wave height, h is the water depth, and $k = 2\pi/\lambda$ is the wave number with λ being the wavelength and determined by the dispersion equation $\omega^2 = gk\tanh kh$.

Wave energy dissipation is assumed to be the work of canopy drag following Zhu et al. (2020a) for which the conservation equation becomes

$$\frac{\partial Ec_g}{\partial x} = -\int_0^l N\alpha_\epsilon \overline{\frac{1}{2}C_{di}\rho b|U_R|U_R^2}ds, \tag{21}$$

where $E = \rho g H^2/8$ is the local wave energy per unit horizontal area, $c_g = \omega(1+2kh/\sinh 2kh)/2k$ is the wave group velocity, N is the canopy density defined as the number of blades per unit horizontal area, $\alpha_\epsilon \le 1$ is a factor to consider the sheltering effects between blades with $\alpha_\epsilon = 1$ for no sheltering, and U_R is the relative velocity normal to the blade with

$$U_R = -w - U\sin\phi + W\cos\phi. \tag{22}$$

As the sheltering effects are considered using the factor α_ϵ, the relative velocity U_R is therefore calculated using the blade normal velocity w of an unsheltered single blade and the incident wave orbital velocity (U, W) without modifications for sheltering effects. Solving (21) with (22) yields the transmitted wave height $H(x)$ at distance x in relation to the incident wave height H_0 at $x = 0$,

$$\frac{H(x)}{H_0} = \frac{1}{1+k_D H_0 x}, \tag{23}$$

where the wave decay coefficient (k_D) is expressed as

$$k_D = \frac{8\alpha_\epsilon bNk^2\sinh^2 kh}{H_0^3\omega^3(2kh+\sinh 2kh)}\int_0^l \overline{C_{di}|U_R|U_R^2}ds. \tag{24}$$

For a rigid blade with $(u, w) = 0$ and $\phi = 3\pi/2$, (24) becomes

$$\begin{aligned} k_{D,R} &= \frac{8\alpha_\epsilon bNk^2\sinh^2 kh}{H_0^3\omega^3(2kh+\sinh 2kh)}\int_0^l \overline{C_{di}|U|U^2}ds \\ &= \frac{\alpha_\epsilon C_{di}bNk}{9\pi} \\ &\cdot\frac{9\sinh k(h-d_1) - 9\sinh k(h-d_1-l) + \sinh 3k(h-d_1) - \sinh 3k(h-d_1-l)}{\sinh kh(2kh+\sinh 2kh)}. \end{aligned} \tag{25}$$

For a sparse canopy with $\alpha_\epsilon = 1$, (25) reduces to the solution by Zhu and Zou (2017), which can be further reduced to the solutions of Dalrymple et al. (1984) and Kobayashi et al. (1993) for bottom-rooted vegetation with $d_1 = h - l$.

Solution (24) for the wave decay coefficient k_D of flexible blades is an implicit expression that requires calculating the relative velocity U_R between blades and waves by resolving the blade motion. Thus, solving (24) is computationally expensive. However, for rigid blades, (24) reduces to an explicit expression, i.e., (25), which is very easy to calculate. In order to obtain a similar explicit expression as (25) for flexible blades, the bulk drag coefficient and effective blade length methods with a rigid blade assumption are used. The assumption of rigid blades can overestimate the wave attenuation for flexible blades. To reduce the overestimation, the bulk drag coefficient (C_{DB}) is therefore defined as a reduced drag ($C_{DB} < C_{di}$) such that $\int_0^l \overline{C_{di}|U_R|U_R^2}ds = \int_0^l \overline{C_{DB}|U|U^2}ds$, yielding

$$\begin{aligned} k_D &= \frac{8\alpha_\epsilon bNk^2\sinh^2 kh}{H_0^3\omega^3(2kh+\sinh 2kh)}\int_0^l \overline{C_{di}|U_R|U_R^2}ds \\ &= \frac{8\alpha_\epsilon bNk^2\sinh^2 kh}{H_0^3\omega^3(2kh+\sinh 2kh)}\int_0^l \overline{C_{DB}|U|U^2}ds \\ &= \frac{\alpha_\epsilon C_{DB}bNk}{9\pi} \\ &\cdot\frac{9\sinh k(h-d_1) - 9\sinh k(h-d_1-l) + \sinh 3k(h-d_1) - \sinh 3k(h-d_1-l)}{\sinh kh(2kh+\sinh 2kh)}. \end{aligned} \tag{26}$$

Similarly, the effective blade length (l_e) is defined as a reduced blade length ($l_e < l$) such that $\int_0^l \overline{C_{di}|U_R|U_R^2}ds = \int_0^{l_e} \overline{C_{di}|U|U^2}ds$, yielding

$$\begin{aligned} k_D &= \frac{8\alpha_\epsilon bNk^2\sinh^2 kh}{H_0^3\omega^3(2kh+\sinh 2kh)}\int_0^l \overline{C_{di}|U_R|U_R^2}ds \\ &= \frac{8\alpha_\epsilon bNk^2\sinh^2 kh}{H_0^3\omega^3(2kh+\sinh 2kh)}\int_0^{l_e} \overline{C_{di}|U|U^2}ds \\ &= \frac{\alpha_\epsilon C_{di}bNk}{9\pi} \\ &\cdot\frac{9\sinh k(h-d_1) - 9\sinh k(h-d_1-l_e) + \sinh 3k(h-d_1) - \sinh 3k(h-d_1-l_e)}{\sinh kh(2kh+\sinh 2kh)}. \end{aligned} \tag{27}$$

The bulk drag coefficient and effective blade length methods are computationally efficient by removing the computation requirements for blade motion. Additionally, the explicit expression is easier to analyze the characteristics of wave attenuation. However, the empirical values of C_{DB} and l_e need to be determined from detailed laboratory experiments. Some empirical formulas for C_{DB} (e.g., Kobayashi et al., 1993; Mendez and Losada, 2004; Augustin et al., 2009; Bradley and Houser, 2009; Sánchez-González et al., 2011; Jadhav et al., 2013;

Anderson and Smith, 2014; Ozeren et al., 2014; Chen et al., 2018; van Veelen et al., 2020) and l_e (e.g., Luhar et al., 2017; Lei and Nepf, 2019a,b) have been developed for submerged canopies. However, a need exists to develop C_{DB} and l_e formulas of suspended canopies for wave attenuation applications.

To quantify the wave attenuation through a canopy with length of L_v, wave transmission ratio (HTR) and wave energy dissipation ratio (EDR) are often used. The wave transmission ratio is defined as the ratio of the wave height at the ending edge of the canopy to the incident wave height and given by

$$HTR = \frac{H(L_v)}{H(0)} = \frac{1}{1 + k_D H_0 L_v}. \tag{28}$$

The wave energy dissipation ratio is defined as the ratio of the dissipated wave energy to the incident wave energy and given by

$$EDR = \frac{H(0)^2 - H(L_v)^2}{H(0)^2} = 1 - HTR^2 = 1 - \frac{1}{(1 + k_D H_0 L_v)^2}. \tag{29}$$

3. Experiments

3.1. Measurements for cultivated S. latissima

The model kelp material is selected based on the properties of the *S. latissima* cultivated on a 60 m kelp aquaculture longline in Saco Bay, Maine, USA. *S. latissima* is one of the most extensively farmed kelp species in Maine and in the USA (Augyte et al., 2017; Breton et al., 2018; Sappati et al., 2019; Grebe et al., 2019; Mao et al., 2020; Grebe et al., 2021). Two sets of kelp samples were collected from two nonadjacent 10 cm regions of the longline on May 17, 2018, with 43 (0.689 kg) and 38 (0.683 kg) samples, respectively. Therefore, the averaged plant density and yield were about 405 plants/m and 6.86 kg/m. The kelp samples were stored in seawater. The morphological and mechanical properties of the kelp samples were measured within 24 h after collection to minimize the effects of kelp deterioration.

S. latissima consists of holdfast, stipe and blade (Fig. 2a). Compared to the dimensions of kelp blade, the holdfast and stipe are small and difficult to match in the physical model. To illustrate this characteristic, consider the 1.90 m-long kelp on Fig. 2a as an example, the stipe length is 15 cm and 8.6% of the blade length at 175 cm. The diameter of the stipe is 5.8 mm and 4.5% of the blade width at 130.4 mm. In a 1:10 physical model, the model stipe diameter is less than 0.58 mm. Thus, the holdfast and stipe are not geometrically modeled in this study. However, the rigid holdfast and stipe are important to fix the blade and therefore affect the blade bending. To model the effects of the holdfast and stipe, the fixed base of the model blade is designed such that the ratio of the length of the fixing base to the length of the flexible part of the model blade is 5.2%, which is comparative to the ratio of the stipe length to the blade length in the field (e.g., 8.6% for the *S. latissima* sample on Fig. 2).

The kelp blade morphological characteristics were measured from 77 samples using a ruler for the blade length, a caliper for the blade width and a micrometer for the blade thickness. The blade width was determined by taking the average from three positions: near the stipe, in the middle and near the tip. Thickness values were obtained along the blade width at intervals of 1.27 cm (0.5 in) with at least five positions.

The mass density and bending elastic modulus were measured from 41 rectangular specimens cut out from 6 to 9 different positions along the blade length of 6 blades. Since the kelp tissue started to degrade and die after cuts were made, the measurements for each specimen were completed within 2 min, and the measurements for one whole kelp blade sample were completed within 1 h. The specimens were cut out from the center part of the blade where the blade thickness varies slightly with an averaged standard deviation of less than 0.5% of the averaged thickness. Thus, the cross section can be considered as a rectangular section and the volume of the specimen can be calculated using the averaged thickness, width and length. The mass of the specimen was measured using a digital balance scale with the precision of 0.1 mg. To control the effects of the wetness of the specimen, the specimen was placed between two layers of a paper towel to reduce the seawater attached on the specimen surface. The specimen was still wet, but not dripping during the measurements. Due to the loss of surface water and kelp degradation, the measured mass values decreased by 4% during the course of the experiment. The averaged mass value was used in this study.

The bending elastic modulus of the kelp blade was measured using the cantilever beam bending test (Fig. 2b). Four bending tests were conducted for each specimen with measurements taken on both ends and both sides, for 164 tests. For each bending test, a photo of the bending blade was taken to record the blade posture. The blade posture was extracted using ImageJ (a Java-based image processing program, Schneider et al., 2012; Liang et al., 2017). Given a value of E, solving (2) and (3) by setting $u = 0$, $w = 0$, and $\rho = 0$ with boundary conditions yields ϕ, which can be used to calculate the blade posture with (16) and (17). The measured E is set as the value with which the calculated blade posture fits best with the measured blade posture (Fig. 2c). The calculated blade postures compared well with the measured blade postures, with $R^2 > 0.95$ for 160 tests and $R^2 = 0.88$, 0.89, 0.92, and 0.93 for the other 4 tests.

3.2. Experimental design

The laboratory experiments were conducted in the 24 m-long, 38 cm-wide, and 60 cm-high wave flume in the Nepf Environmental Fluid Mechanics Lab at Massachusetts Institute of Technology in August 2018. The model experiments were designed at a scale of 1:10 to match the dimensions of the wave flume. The wave conditions were designed based on Froude similarity. The model kelp blade was made to satisfy the similarity for (6) to (12).

In the physical model experiments, the holdfast, stipe, the ruffle of the kelp blade, and the variance of thickness were too small to scale so that the kelp was modeled as a rectangular flat plate with a constant thickness. The material selected for modeling kelp blades was silicon film with $\rho_v = 1.20$ g/cm^3, $E = 2.04$ MPa, and $d = 0.10$ mm. The model kelp was designed as a 10.16 cm (4 in) long and 0.95 cm (3/8 in) wide rectangular plate. The fixed part of the blade was $l_r = 0.5$ cm so that the flexible part of the blade was $l_f = 9.66$ cm with $l_r/l_f = 5.2\%$. It is noted that the fixed part of the blade is to model the effects of kelp stipe and the flexible part of the blade is to model the kelp blade. Thus, the corresponding full-scale kelp blade was 96.6 cm long, 9.5 cm wide and 1.0 mm thick. To satisfy dynamical similarity, the mass density and bending elastic modulus of the full scale kelp blade were designed as $\rho_v = 1.23$ g/cm^3 and $E = 21.0$ MPa, such that

$$\frac{(\rho')_M}{(\rho')_F} = 1,\ \frac{(B)_M}{(B)_F} = 1,\ \frac{(Ca)_M}{(Ca)_F} = 1,\ \frac{(L)_M}{(L)_F} = 1,\ \frac{(\delta)_M}{(\delta)_F} = 1,\ \frac{(KC)_M}{(KC)_F} = 1,\ \text{and}\ \frac{(S)_M}{(S)_F} = 1, \tag{30}$$

where the subscript $(\,)_M$ denotes the dimensionless parameter for the model and $(\,)_F$ denotes the dimensionless parameter for the full scale prototype. The properties of the full-scale model blade will be compared with the measurements for *S. latissima* blade in Section 4.1.

A kelp farm includes numerous kelp plants attached to a horizontal rope. In this laboratory experiment, the horizontal rope was modeled using a rigid stainless steel welding rod with a diameter of 0.89 mm (0.035 in). For each model longline, 31 aggregates of model kelp blades with 10 blades for each aggregate were fixed to the model longline (Fig. 3a).

The plant density for the model longline was 10 plants/cm equivalent to 100 plants/m for the full scale, which was less than the measured values at 405 plants/m in this study. The rod was mounted to a stainless steel frame attached to the flume walls (Fig. 3b). The model

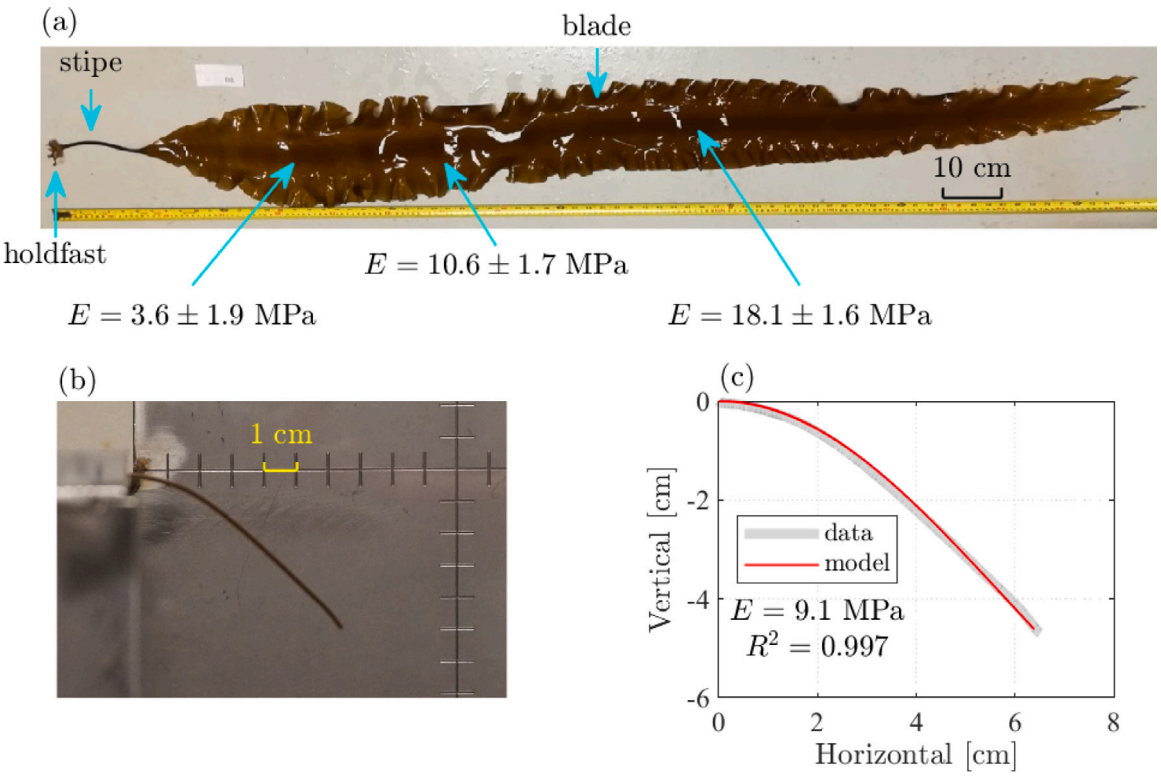

Fig. 2. (a) *Saccharina latissima* sample with bending elastic modulus (E) at three positions along the blade length. (b) Bending test for a specimen. (c) Comparison between the measured and calculated blade postures. The measured E is the value with which the calculated blade posture has the largest R^2 compared with the data. Photo credit: Yu-Ying Chen.

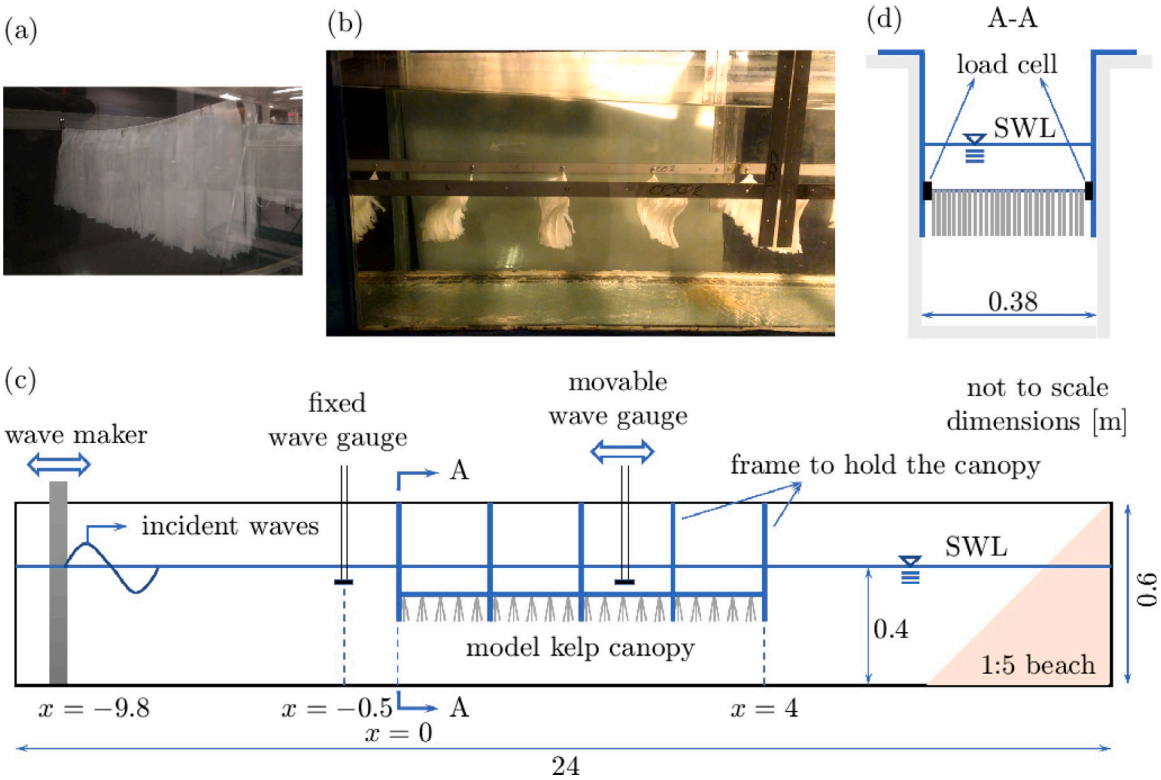

Fig. 3. Photos of (a) a model kelp longline and (b) the model kelp farms with waves propagating from left to right (see video S2 for the video in the supplementary materials). Sketches of (c) the side view of the wave flume showing the setup of model kelp farms and wave gauges and (d) the front view of section A-A showing the setup of load cells.

kelp farm consisted of 20 model sections with a distance of 20 cm apart in the flume. Thus, the total canopy length was $L_v = 3.8$ m equivalent to 38 m in the full scale. The canopy density N was 5263 plants/m^2.

Three vertical positions of the model kelp farm beneath the SWL with $d_1 = 6$, 11, and 16 cm were compared in the experiments.

A set of experiments were then conducted to investigate the dynamics of a single blade and a blade in the canopy with a water depth of 40 cm. The suspended blade was fixed at 11 cm below the SWL. The wave height ranged from 1.4 cm to 6 cm with 4 wave periods of 0.8 s, 1 s, 1.4 s, and 2 s. The blade motion was recorded by a Canon 5D Mark III camera for 10 wave periods at 50 frames per second. The videos were processed using MATLAB R2019b.

After the blade dynamics were investigated, another set of experiments was then conducted to assess the wave attenuation. As the suspended blades were observed to roll over the attached rod in large wave heights, the largest wave heights were set at 3.8 cm to prevent the blade roll over the attachment in the wave attenuation experiments. For the wave attenuation experiments, the incident wave height was $H_{I0} = 1.8$–3.8 cm, wave period was $T_w = 0.8$–2 s, water depth was $h = 30$–40 cm, and wavelength was $\lambda = 103$–369 cm with $\lambda/h = 2.7$–10.9, $H_{I0}/h = 0.05$–0.11, $l_f/h = 0.24$–0.32, and $d_1/h = 0.2$–0.4. The canopy covered 1 to 3.7 wavelengths. Thus, for the equivalent full-scale model, the waves were 18 cm to 38 cm in height with period of 2.6 to 6.3 s in 3 to 4 m-deep water. To calculate Re, KC, Ca, and L, as well as the hydrodynamic coefficients C_f, C_{di}, and C_m, the horizontal wave orbital velocity at the fixed end of the flexible part of the blade was used, yielding $Re = 406$–861, $KC = 4.4$–18.8, $Ca = 9667$–43406, $L = 3.4$–14.4, $C_f = 0.02$, $C_{di} = 3.8$–6.1, and $C_m = 1$–2.5. A total of 14 cases were run with the detailed characteristics shown in Table 1.

3.3. Wave decay measurements

The wave decay experiment setup is shown on Fig. 3. During the tests, the wave height was measured using two resistance-type wave gauges with one permanently mounted at 50 cm before the canopy and the other moving along the canopy to measure the wave height evolution for each case. The fixed wave gauge provided a reference measurement to show that the wave conditions were steady throughout one case. The movable wave gauge collected data along the canopy at an interval of 5 cm or up to 15 cm depending on the wavelength (with at least 20 horizontal positions for one wavelength). At each horizontal position, the wave gauge measured the water elevation at 1000 Hz for 1 min (including 30 to 74 wave periods).

The wave reflection ratio of the flume is estimated at 7% (Lei and Nepf, 2019b), yielding an oscillating wave height along the canopy (Fig. 4). Assuming that the incident wave height and reflected wave height decay follow (23) at the same decay coefficient k_D along the canopy, a local wave height in the canopy can be obtained by (31) given in Box I (with derivation in Appendix A). In (31), H_{I0} is the incident wave height at $x = 0$, H_{RL_v} is the reflected wave height at $x = L_v$, and ϵ is the phase lag. The spatial oscillation period of the wave height is 1/2 wavelength as shown in the term $\cos(2kx + \epsilon)$. Eq. (31) provided a good fit ($R^2 > 0.99$) for the incident wave height and decay coefficient with the nonlinear regression model 'fitnlm' in MATLAB R2019b as shown on Fig. 4. The flume bottom and walls as well as the kelp supporting frames can also induce wave decay (Fig. 4). According to Madsen et al. (1988), the wave energy dissipation by the friction of the flume bottom and walls is proportional to the cubic of the maximum orbital velocity near the bottom and walls with a similar expression to the wave energy dissipation by vegetation in (21), yielding the same wave height transmission in (23) but with a different wave decay coefficient due to the flume bottom and walls. Therefore, the wave decay coefficient over the wave flume without kelp can be also fitted using (31). Since this study focuses on the wave attenuation due to kelp canopies, the wave decay coefficient due to the flume bottom and walls as well as the kelp supporting frames is subtracted from the measured wave decay coefficient for the kelp canopy in the following analysis.

The model kelp farms consisted of 20 rows (rods) of blades. The rods were 20 cm apart, which was more than four times of the amplitude of the blade deflection. For each row, 31 aggregates of blades were attached separately with 1 aggregate/cm (Fig. 3a). For each aggregate, 10 blades were mounted together so that the front blades sheltered the blades behind them. The sheltering effects between rods were not considered in this study. However, the sheltering effects between the blades in the same aggregate were significant and considered using a sheltering factor. The sheltering effects for the drag force can be considered using the force ratio of the sheltered and unsheltered blades given by

$$\alpha_F = \frac{F_{x,rms}}{\beta_n f_{x,rms}}, \tag{32}$$

where $F_{x,rms}$ is the root-mean-square (RMS) of the measured horizontal force on one row of aggregates of sheltered blades, $f_{x,rms}$ is the RMS of the measured horizontal force on one row of unsheltered single blades, and β_n is the ratio of the number of sheltered blades to the number of unsheltered blades, i.e., the number of blades in one aggregate. It is noted that the wave energy dissipation is proportional to U_R^3 in (21) while the drag force is proportional to U_R^2. Therefore, the sheltering factor α_ϵ used in the calculation of the wave attenuation is defined as

$$\alpha_\epsilon = \alpha_F^{3/2} \tag{33}$$

with the force ratio α_F given by (32). To measure the total horizontal force on one row of blades, two submerged load cells were mounted to both ends of the rod (Fig. 3d) and recorded at 2000 Hz for 1 min at the same time. The total force is the sum of the forces at both ends. Similar to the measurement of k_D, the measured "forces" without kelp were subtracted from the measured forces with kelp under the same wave conditions. In this study, $f_{x,rms}$ was measured for 30 isolated blades on one rod and $F_{x,rms}$ was measured for 30 aggregates of 10 sheltered blades, i.e., totally 300 blades on one row. Therefore, β_n was 10 in this study.

4. Results

4.1. Morphological and mechanical properties of S. latissima compared with the model blade

To evaluate the design of model kelp blade, the results section begins with understanding the morphological and mechanical properties of real cultivated *S. latissima* in Saco Bay, Maine of the USA. The kelp blade length (l_f) showed a quasi-linear relationship with the averaged blade width (b) as

$$b = (0.090 \pm 0.003) l_f + 1.4 \pm 0.2, \tag{34}$$

with $R^2 = 0.90$ (Fig. 5a), where l_f and b are in cm. The blade width has the following relation with the maximum thickness ($d_{\max}$) at the center of the blade width,

$$d_{\max} = (0.040 \pm 0.007) b + 0.39 \pm 0.08, \tag{35}$$

with $R^2 = 0.75$ (Fig. 5b), where $d_{\max}$ is in mm while b is in cm. The blade thickness (d) showed a normal-like distribution along the blade width following

$$\frac{d}{d_{\max}} = (0.797 \pm 0.011) e^{-\frac{1}{2}\left(\frac{s_b/b}{0.118 \pm 0.003}\right)^2} + 0.203 \pm 0.011, \tag{36}$$

with $R^2 = 0.94$ (Fig. 5c), where s_b is the distance from the center of the blade width toward the blade edge.

The bending elastic modulus increases along the blade length from near the stipe to near the tip (Fig. 2a). As more mature elements of the blade are near the tip, E is expected to relate to the maturity of the kelp tissue. The relation between E and $d_{\max}$ is

$$E = (2.3 \pm 1.2) d_{\max}^{16 \pm 7} + 5.5 \pm 0.7, \tag{37}$$

Table 1
Wave conditions and hydrodynamic coefficients for the model kelp canopy in the experiments. In this table, d_1 is the vertical location of the longlines from the still water level, h is the water depth, T_w is the wave period, H_{I0} is the incident wave height, λ is the wavelength, U_m is the magnitude of the horizontal wave orbital velocity at the fixed end of the blade, l_f is length of the flexible part of the blade, L_v is the canopy length, Re is the Reynolds number, KC is the Keulegan–Carpenter number, Ca is the Cauchy number, L is the length ratio, C_{di} is the individual drag coefficient, C_f is the friction coefficient, and C_m is the added mass coefficient.

Case #	d_1 [cm]	h [cm]	T_w [s]	H_{I0} [cm]	λ [cm]	U_m [cm/s]	l_f/h	L_v/λ	d_1/h	λ/h	H_{I0}/h	Re	KC	Ca	L	C_{di}	C_f	C_m
1	11	40	1.4	1.8	246	4.3	0.24	1.5	0.28	6.1	0.05	406	6.4	9667	10.0	5.4	0.02	2.2
2	6	30	2.0	2.9	326	8.2	0.32	1.2	0.20	10.9	0.10	783	17.3	35 894	3.7	3.9	0.02	1.0
3	11	40	1.4	2.4	246	5.7	0.24	1.5	0.28	6.1	0.06	545	8.6	17 360	7.4	4.9	0.02	2.5
4	6	30	1.4	2.9	221	8.2	0.32	1.7	0.20	7.4	0.10	778	12.2	35 383	5.2	4.3	0.02	1.7
5	11	40	1.0	3.1	146	6.8	0.24	2.6	0.28	3.7	0.08	646	7.1	24 407	9.0	5.2	0.02	2.3
6	11	40	2.0	3.5	369	8.4	0.24	1.0	0.28	9.2	0.09	798	17.6	37 217	3.6	3.8	0.02	1.0
7	16	40	2.0	3.8	369	8.7	0.24	1.0	0.40	9.2	0.09	831	18.3	40 419	3.5	3.8	0.02	1.0
8	11	40	2.0	3.7	369	9.0	0.24	1.0	0.28	9.2	0.09	855	18.8	42 773	3.4	3.8	0.02	1.0
9	16	40	1.4	3.2	246	7.0	0.24	1.5	0.40	6.1	0.08	669	10.5	26 192	6.0	4.6	0.02	2.1
10	11	40	1.4	3.2	246	7.6	0.24	1.5	0.28	6.1	0.08	719	11.3	30 272	5.6	4.5	0.02	1.9
11	11	40	1.0	3.6	146	7.9	0.24	2.6	0.28	3.7	0.09	754	8.3	33 252	7.7	4.9	0.02	2.4
12	6	30	0.8	3.2	103	9.0	0.32	3.7	0.20	3.4	0.11	861	7.9	43 406	8.1	5.0	0.02	2.4
13	16	40	0.8	3.2	107	5.1	0.24	3.6	0.40	2.7	0.08	483	4.4	13 642	14.4	6.1	0.02	1.9
14	11	40	0.8	3.2	107	6.6	0.24	3.6	0.28	2.7	0.08	632	5.8	23 369	11.0	5.6	0.02	2.1

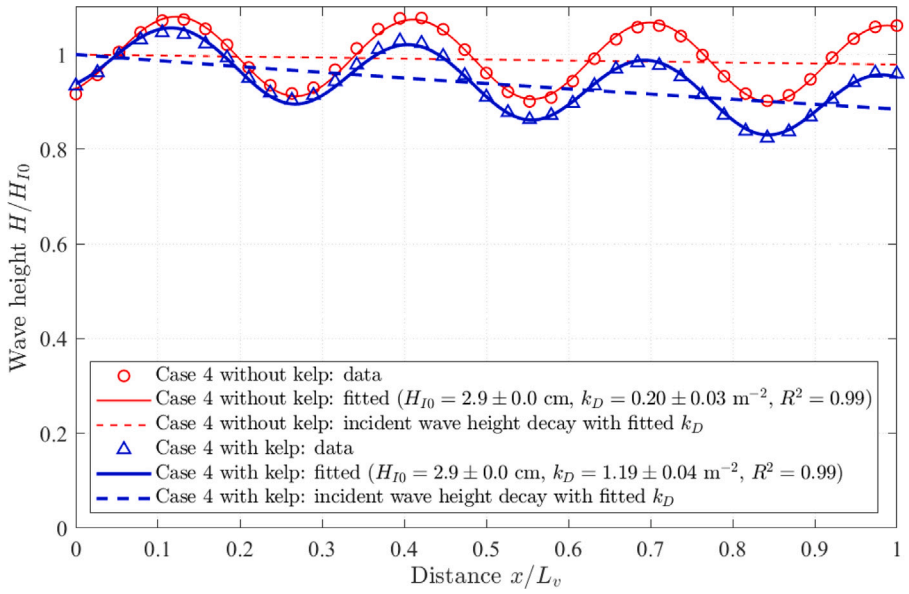

Fig. 4. Measured (red circles for that without kelp and blue triangles for that with kelp) and fitted (solid lines, $R^2 = 0.99$) wave heights (H) normalized by the incident wave height (H_{I0}) along the model kelp farms for Case 4. The calculated incident wave height decay with fitted H_{I0} and k_D is denoted by dashed lines. The red thin lines are for the case without kelp while the blue thick lines are for the case with kelp. The horizontal distance is normalized by the canopy length as x/L_v.

$$H(x) = \sqrt{\left(\frac{H_{I0}}{1 + k_D H_{I0} x}\right)^2 + \left[\frac{H_{RL_v}}{1 + k_D H_{RL_v}(L_v - x)}\right]^2 + 2\frac{H_{I0}}{1 + k_D H_{I0} x}\frac{H_{RL_v}}{1 + k_D H_{RL_v}(L_v - x)}\cos(2kx + \epsilon)}, \tag{31}$$

Box I.

with $R^2 = 0.41$ (Fig. 5d), where $d_{\max}$ is in mm and E is in MPa. The measured E from all specimens ranges from 2.7 ± 1.4 to 22 ± 6 MPa (Fig. 5d). The measurements in Vettori and Nikora (2017) and Fredriksson et al. (2020) with 4 ± 3 MPa and 1.3 ± 0.4 MPa, respectively, are also in this range.

The measured mass density of *S. latissima* is 1.05 ± 0.03 g/cm^3, which is smaller than the measurement in Fredriksson et al. (2020) with 1.3 ± 0.3 g/cm^3, but comparable to the value of 1.09 ± 0.09 g/cm^3 in Vettori and Nikora (2017). The difference may be caused by the "wetness" of the kelp sample since the measured mass of wetter kelp is larger, resulting in a larger mass density. The measurements are summarized in Table 2 along with the measurements from published literature.

The designed properties of the full-scale model kelp blade are also shown in Table 2 to compare with the measurements in this study and from published literature. Based on the measurements, for a given kelp blade length $l_f = 96.6$ cm, the expected blade width is $b = 10.1 \pm 0.5$ cm using (34), the maximum blade thickness is $d_{max} = 0.79 \pm 0.17$ mm using (35), and the bending elastic modulus is $E = 5.6 \pm 0.8$ MPa using (37). The designed width ($b = 9.5$ cm) of the full-scale model blade is slightly smaller than the calculated averaged width ($b = 10.1 \pm 0.5$ cm) of *S. latissima* with the same blade length, while the maximum thickness

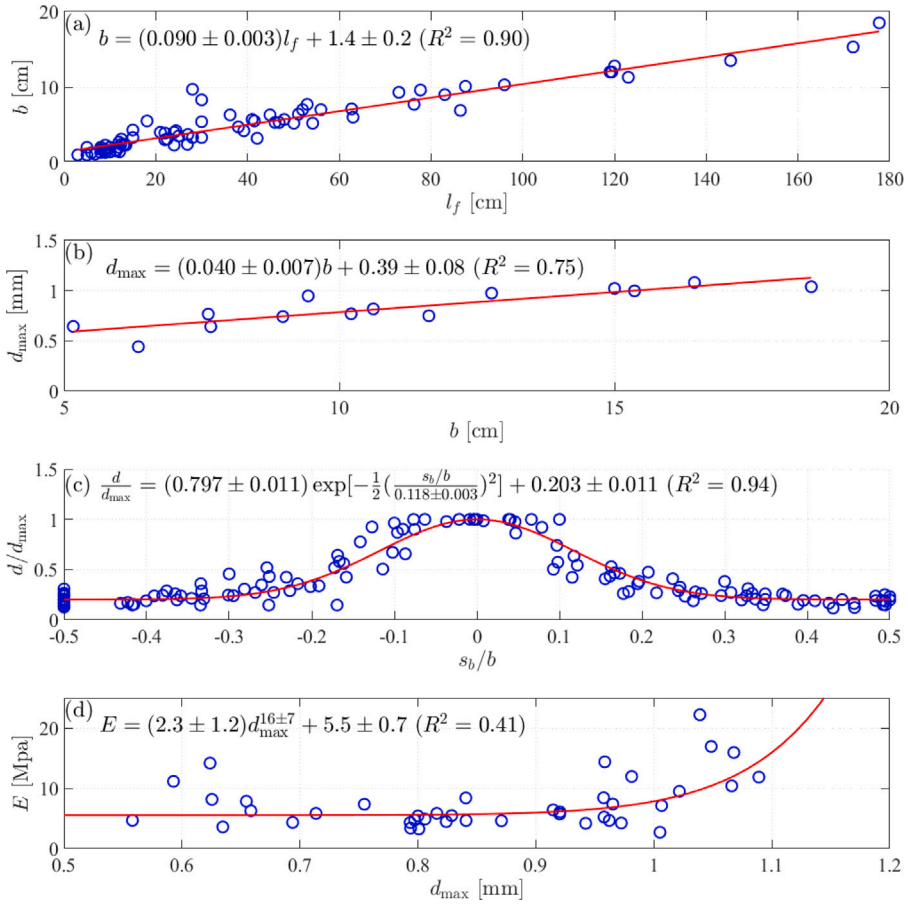

Fig. 5. Morphological and mechanical properties of *S. latissima*. (a) Relation between the averaged blade width (b) and the blade length (l_f). (b) Relation between the maximum thickness ($d_{\max}$) and the averaged blade width. (c) The distribution of the normalized blade thickness ($d/d_{\max}$) along the normalized distance (s_b/b) from the blade center. (d) Bending elastic modulus (E).

Table 2
Morphological and mechanical properties of cultivated *S. latissima* and model kelp blades.

	Study site	Mass density ρ_v [g/cm^3]	Elastic modulus E [MPa]	Blade length l_f [cm]	Blade width b [cm]	Maximum blade thickness $d_{\max}$ [mm]	Blades per meter [m^{-1}]
Model kelp blade (scale 1:10)		1.2	2.04	9.66	0.95	0.10	1000
Designed full-scale kelp blade		1.23	21.0	96.6	9.5	1.0	100
Measured values in this study	Saco, Maine, US	1.05 ± 0.03	5.6 ± 0.8[c] ($2.7 \pm 1.4 - 22 \pm 6$)	96.6 (3 – 177.7)	10.1 ± 0.5[a] (1 – 18.5)	0.79 ± 0.17[b] (0.44 – 1.08)	405
Fredriksson et al. (2020)	Maine, US	1.3 ± 0.3	1.3 ± 0.4	Up to 300	–	0.4 ± 0.1	–
Vettori and Nikora (2017)	Loch Fyne, Scotland, UK	1.09 ± 0.09	4 ± 3	15 – 65	3.6 – 13.1	0.42 – 1.8	–
Augyte et al. (2017)	Bristol, Maine, US	–	–	220.4[d]	4.67[d]	–	330[d]
		–	–	56.9	8.72	–	–
	Sorrento, Maine, US	–	–	147.4[d]	2.76[d]	–	400[d]
		–	–	71.4	7.38	–	–
Peteiro and Freire (2013)	Ares, Spain	–	–	152.9	12.1	–	745
	Sada, Spain	–	–	123.2	11.4	–	728

[a]Calculated b using (34) for the given $l_f = 96.6$ cm.
[b]Calculated $d_{\max}$ using (35) for given $b = 10.1 \pm 0.5$ cm.
[c]Calculated E using (37) for given $d = 0.79 \pm 0.17$ mm.
[d]Narrow-bladed kelp.

($d_{\max}$ = 1.0 mm) is slightly larger than that ($d_{\max} = 0.79 \pm 0.17$ mm) of the real *S. latissima*. However, the designed dimensions of the full scale kelp blade are within the range of the measurements as shown in Table 2. The designed mass density (ρ_v = 1.23 g/cm^3) of the full-scale model blade is larger than the measured value of 1.05 ± 0.03 g/cm^3, but comparable to the measurement in Fredriksson et al. (2020) with 1.3±0.3 g/cm^3 for cultivated *S. latissima* in Maine. The designed bending elastic modulus E = 21.0 MPa of the full-scale model kelp blade is large but still within the range of the measurements (2.7 ± 1.4 to 22 ± 6 MPa). The designed plant density 100 plants/m is smaller than the measured value of 405 plants/m.

4.2. Wave-induced motion of suspended blades

To understand the wave-induced dynamics of suspended blades as well as the sheltering effects among blades, the motion of a single suspended blade is compared with that of an aggregate of suspended blades on Fig. 6 (with video S3 in the supplementary materials), where

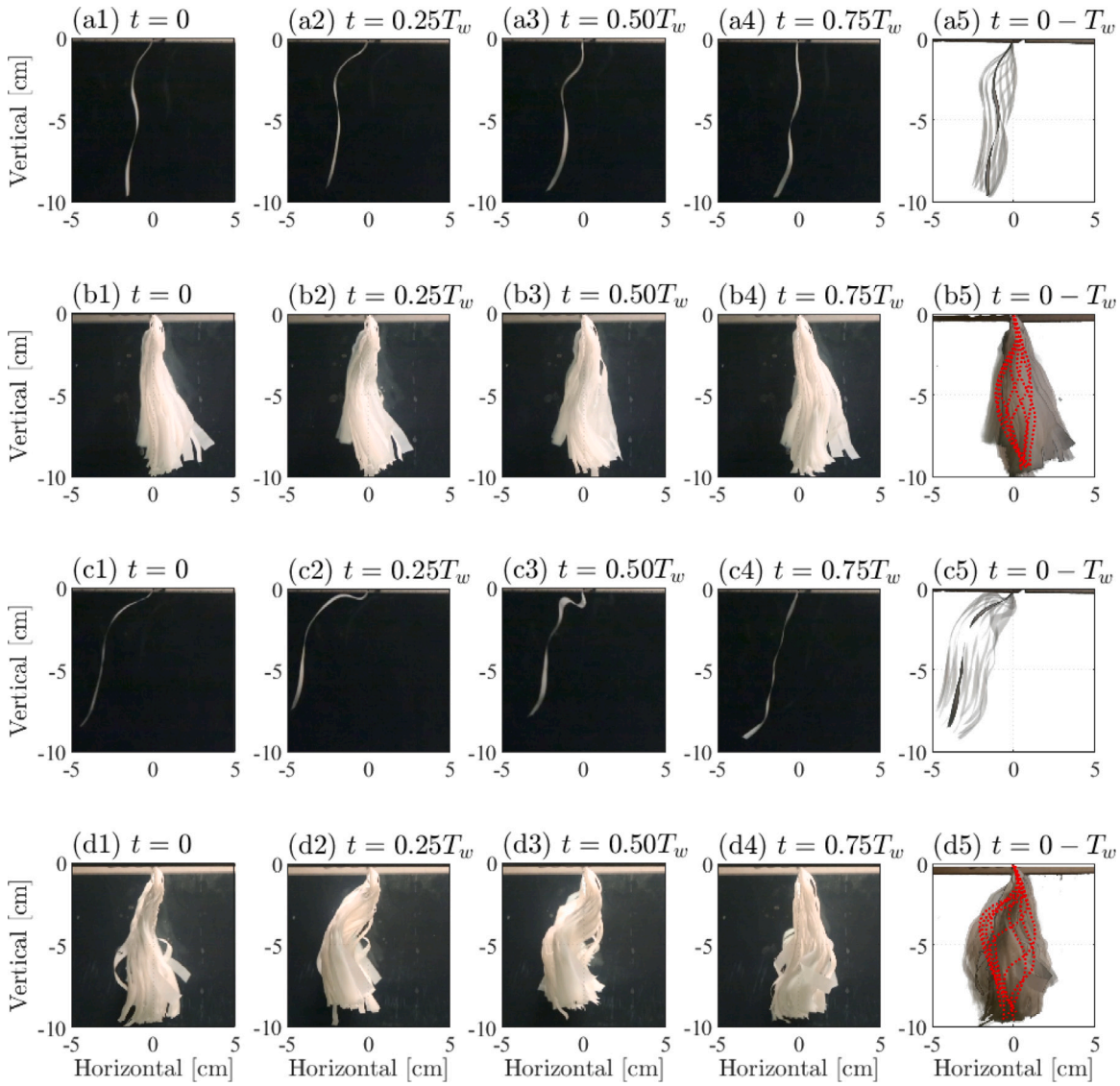

Fig. 6. Postures for (a and c) a single blade and (b and d) a row of blades in waves with wave heights of (a and b) 1.5 cm and (c and d) 2.8 cm, respectively. The wave period (T_w) is 1.4 s and water depth is 40 cm. The blade is fixed at 11 cm below the still water level. The waves propagate from left to right. The left four columns show the blade posture at one phase. The fifth column shows the blade postures for 12 phases in one wave period with the black line indicates the posture at $t = 0$ and $t = T_w$ while the gray lines indicate the postures at other phases. In (b5) and (d5), the red dotted lines indicate the postures of one representative blade in an aggregate of blades. See video S3 for the video in the supplementary materials.

the waves propagate from left to right with a period of 1.4 s at 40 cm water depth. Due to high flexibility, the blade shows a higher-mode ($\geq$ 3) motion (Fig. 6a and c) with large asymmetry (Fig. 6a5 and c5). Unlike bottom-fixed vegetation inclining to the wave propagation direction (Zhu et al., 2020b), the suspended blade fixed at the upper end inclines to the opposite direction of wave propagation. For waves propagating to the right, the action of the vertical wave orbital velocity on the blade provides clockwise momentum that drives the bottom-fixed blade also to the right (Zhu et al., 2020b) but drives the suspended blade to the left. The asymmetry of blade motion increases with blade deflection and wave height (Fig. 6a and c). More information about the mechanisms and properties of asymmetric blade motion in waves can be found in Zhu et al. (2020b).

The motion of the blade in an aggregate of blades shows a smaller-amplitude motion than a single blade in the same wave conditions (e.g., Fig. 6a and b). This is caused by the sheltering from neighboring blades in the same aggregate, which reduces the flow velocity to the sheltered blades. Therefore, the deflection of a sheltered blade is smaller than that of an unsheltered single blade. Accordingly, the motion asymmetry of the sheltered blade is also smaller than that of the unsheltered single blade (e.g., Fig. 6a and b).

The blade was observed to wrap up and roll over the attached line when the wave height exceeded a critical value (Fig. 7 with video S4 in the supplementary materials). The unsheltered single blade rolled over when the wave height reached 2.8 cm for T_w = 2 s, 3.3 cm for T_w = 1.4 s (Fig. 7), 3.7 cm for T_w = 1 s, and 3.5 cm for T_w = 0.8 s. Due to sheltering effects, the threshold values increased for the sheltered blades in an aggregate, especially for the blade in the center of the aggregate that was sheltered by more blades.

The roll-over motion of the suspended blade results from the asymmetric blade motion driven by the wave orbital motion. When the wave height increases to a critical value, the asymmetry of the blade motion becomes so large that the blade is almost horizontal, providing conditions for the onset of rolling over.

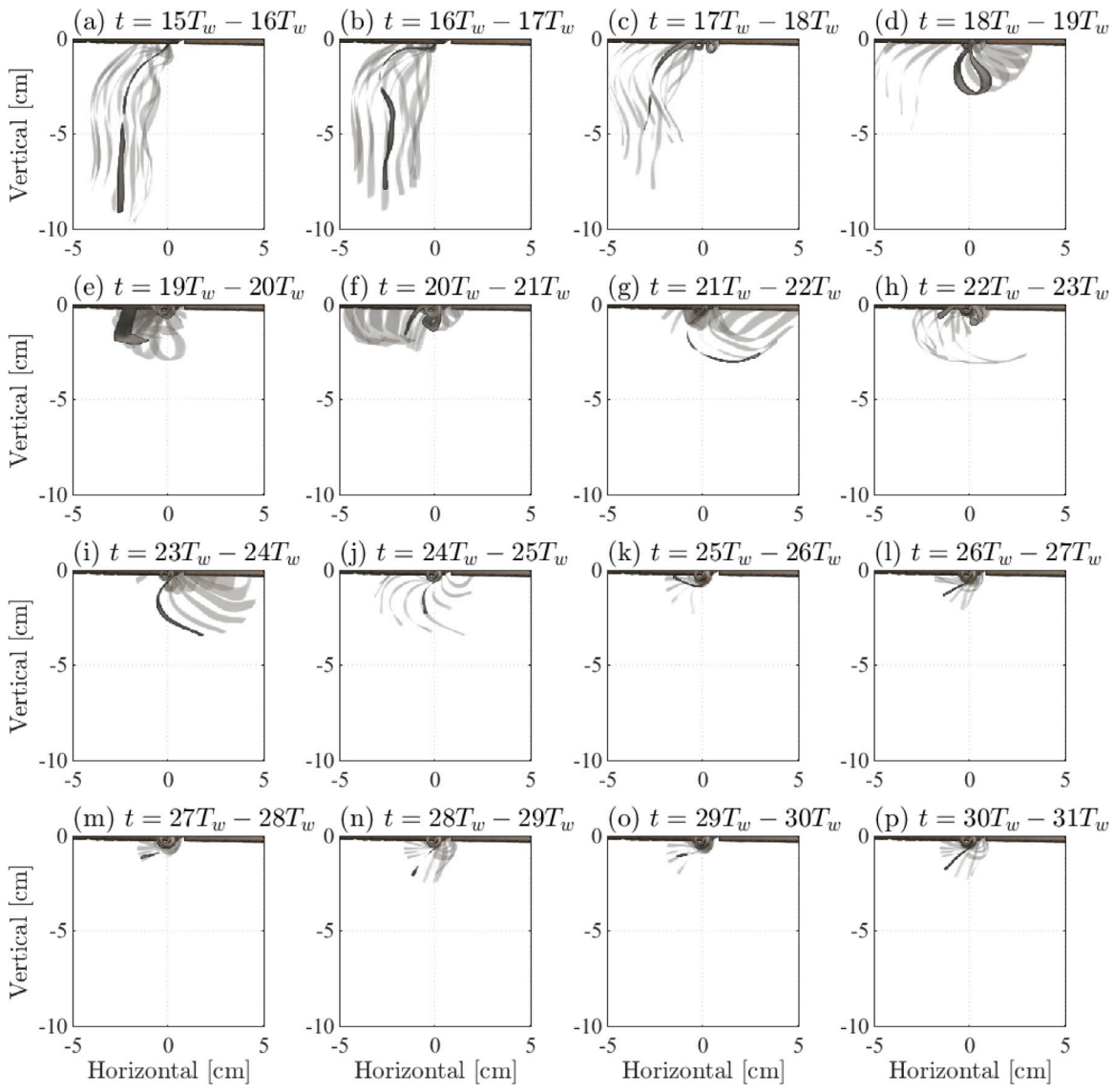

Fig. 7. Postures for a single blade in waves with wave height of 3.3 cm. The wave period (T_w) is 1.4 s and water depth is 40 cm. The blade is fixed at 11 cm below the still water level. The waves propagate from left to right. The black line indicates the posture at the end of the given time (t) while the gray lines indicate the previous postures in that wave period. The blade starts to wrap up and roll over the attached line in the 18th wave period (c) and continue to roll over the attached line again until reaching a steady state after 26 wave periods (k–p). See video S4 for the video in the supplementary materials.

To demonstrate the mechanisms that drive the suspended blade to roll over the attached line, the blade motion (Fig. 7) at representative phases is analyzed with the corresponding wave orbital motion (Fig. 8). As shown on Fig. 8, the blade is almost horizontal at the 17th period. At time $t = 17.25T_w$ (Fig. 8c), the wave orbital velocity points upward and drives the blade to bend upward and exceeds where the fixed end is located. After $t = 17.5T_w$, the wave orbital velocity points to the right and drives the blade to the right (Fig. 8e) to pass over the attachment (Fig. 8f). Then at $t = 17.75T_w$ (Fig. 8g), the wave orbital velocity points downward and drives the blade downward. Therefore, the portion of the blade that passed over the attachment moves down below the attachment. Although the wave orbital velocity changes direction back toward after $t = 17.75T_w$, the blade does not unravel due to the presence of the longline (Fig. 8h). After $t = 18.375T_w$, the restoring force induced by the second curvature of the blade acts clockwise in the same direction of the wave orbital motion. Thus, the blade passes the longline in a shape like a "fly casting loop" (Fig. 8l to p). The whole blade rolls over the longline by the 18th period. In the following time, the blade rolls over the blade again (Fig. 7) until reaching a steady state.

4.3. Horizontal force and wave attenuation

The measured force ratio α_F, sheltering factor α_ϵ, wave decay coefficient k_D, wave transmission ratio (HTR), and wave energy dissipation ratio (EDR) are listed in Table 3. As α_F and α_ϵ are expected to be less than 1, the values $\alpha_F = 1.536$ and $\alpha_\epsilon = 1.904$ for Case 12 are so large that they may be not correct. Additionally, removing these single values would not significantly impact the mean values of α_F and α_ϵ. Thus, they were not used in this study. The rest measured α_F ranging from 0.506 to 1.031 with the mean value $\overline{\alpha_F} = 0.724$ and α_ϵ ranging from 0.360 to 1.047 with the mean value $\overline{\alpha_\epsilon} = 0.630$ were used in the numerical calculations for $F_{x,rms}$ and k_D.

To obtain the numerical simulations for $F_{x,rms}$ and k_D, the input wave field (U, W) were estimated using linear wave theory (19) and (20), which provided a good approximation with $R^2 = 0.91$ for the waves in the flume of this study (Luhar and Nepf, 2016), especially

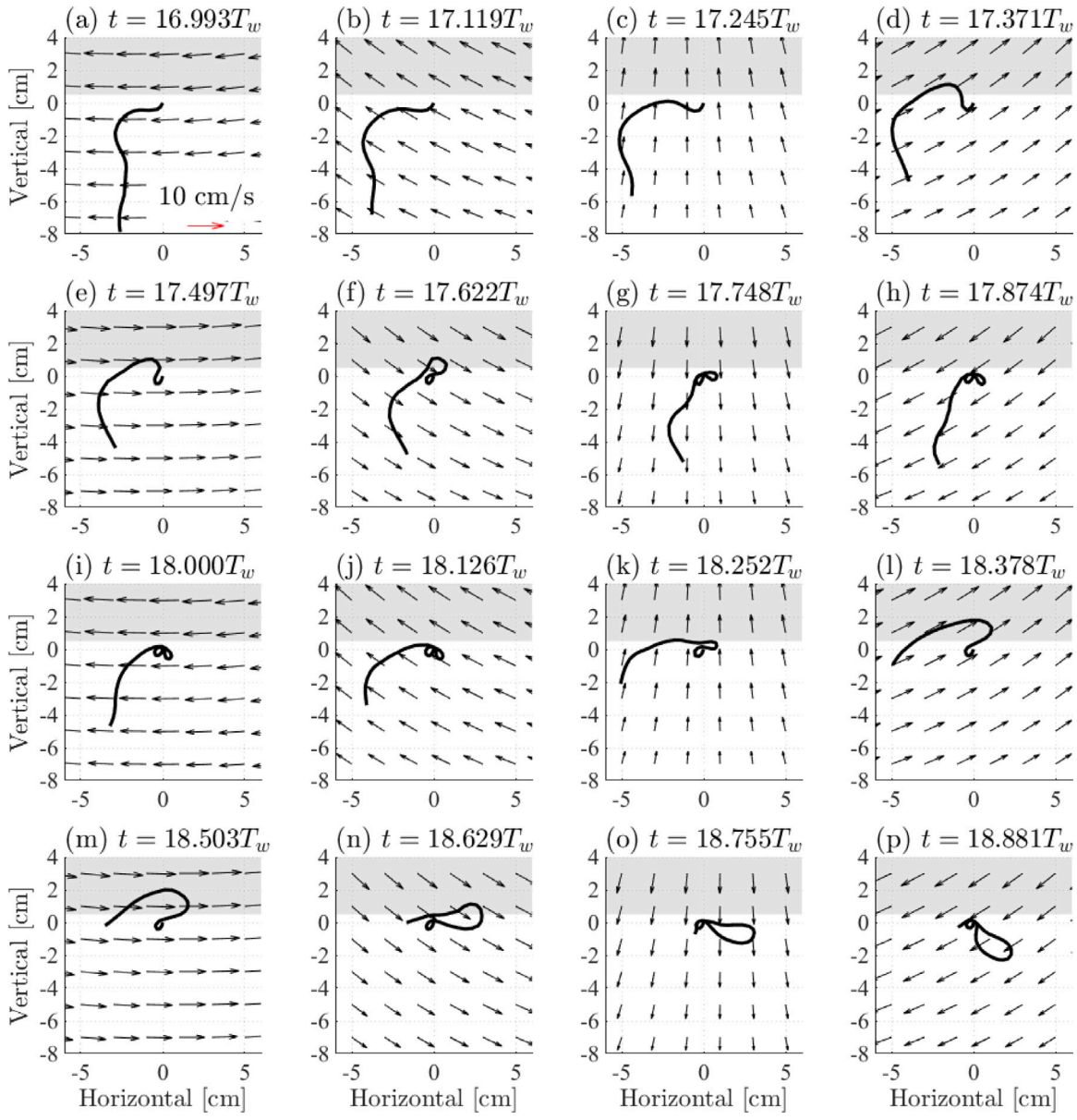

Fig. 8. Suspended blade postures with flow field. The waves propagate from left to right with wave height of 3.3 cm and wave period $T_w = 1.4$ s at water depth of 40 cm. The flow field is calculated using linear wave theory (Dean and Dalrymple, 1991). The blade is fixed at 11 cm below the still water level. The blade starts to roll over the longline at time $t = 17.5T_w$ for this case (e). The shaded regions indicate the position of the supporting frame. The part of the blade in the shaded region was plotted using a smoothing curve that connect the visible blade segments. This does not impact the analysis on the mechanisms for the rolling over of suspended blades. See video S4 for the video in the supplementary materials.

for small-amplitude waves. Since the blade included a rigid part (l_r) and a flexible part (l_f), the computation for k_D (24) was split into two parts, i.e., the wave decay coefficient k_{Dr} for the rigid part as an integral over $[0, l_r]$, and the wave decay coefficient k_{Df} for the flexible part as an integral over $[l_r, l]$ according to the property of the integral. The integral over $[0, l_r]$ for the rigid part was reduced to (25) with $l = l_r$ while the integral over $[l_r, l]$ for the flexible part was still (24) with $l = l_f$. As the rigid parts of the blades in the same aggregate were fixed together, the rigid parts in the same aggregate were considered as one element such that the canopy density for the rigid parts was 526.3 elements/m^2 (i.e., 526.3 aggregates/m^2) and the sheltering effects among the elements were negligible. Thus, k_{Dr} was calculated using (25) with $l = l_r$, $N = 526.3$ m^{-2}, $\alpha_\epsilon = 1$, and C_{di} in Table 1 calculated using (14). For the flexible part, the blade motion was obtained by solving the blade dynamical equations (2) to (5) with (U, W) and the corresponding initial and boundary conditions, yielding the blade velocity (u, w) and direction angle ϕ. In the computation for the blade motion, the used friction coefficient C_f, drag coefficient C_{di}, and added mass coefficient C_m are shown in Table 1, which were calculated using (13), (14), and (15) with the magnitude of the horizontal wave orbital velocity at the fixed end of the flexible part of the blade. With the blade normal velocity w and the wave orbital velocity (U, W), the relative velocity U_R between the blade and the flow was obtained using (22). Then k_{Df} was calculated using (24) with the calculated U_R, $l = l_f$, $N = 5263$ m^{-2}, $\alpha_\epsilon = 0.630$, and C_{di} in Table 1 calculated using (14). Finally, the wave decay coefficient k_D for the kelp canopy was obtained by $k_D = k_{Dr} + k_{Df}$.

Similarly, the computation for $F_{x,rms}$ was also split into two processes, i.e., the drag force for the rigid part and the horizontal force for the flexible part. With the directional angle ϕ obtained from solving the governing equations (2) to (5) for blade motion, the shear force at the fixed end of the flexible part of the blade $Q(s = 0)$ (which is

Table 3
Measurements for the 1:10 scale model experiments and projections to the full scale prototype. In this table, d_1 is the vertical location of the longlines from the still water level, h is the water depth, T_w is the wave period, H_{I0} is the incident wave height, k_D is the wave decay coefficient, α_F is the force ratio, α_ϵ is the sheltering factor, C_{DB} is the bulk drag coefficient, $l_{f,e}$ is the effective blade length for the flexible part of the blade (l_f), HTR is the wave height transmission ratio, and EDR is the wave energy dissipation ratio.

Case	Experiments (1:10)					Projections to full scale					α_F	α_ϵ	C_{DB}	$l_{f,e}/l_f$	HTR	EDR
#	d_1 [cm]	h [cm]	T_w [s]	H_{I0} [cm]	k_D [m^{-2}]	d_1 [m]	h [m]	T_w [s]	H_{I0} [m]	k_D [m^{-2}]						
1	11	40	1.4	1.8	1.22	1.1	4	4.5	0.18	0.0122	0.506	0.360	0.55	0.085	0.92	15.0%
2	6	30	2.0	2.9	0.85	0.6	3	6.3	0.29	0.0085	0.966	0.950	0.20	0.046	0.91	16.3%
3	11	40	1.4	2.4	0.85	1.1	4	4.5	0.24	0.0085	0.511	0.365	0.37	0.063	0.93	14.0%
4	6	30	1.4	2.9	1.00	0.6	3	4.5	0.29	0.0100	0.845	0.776	0.22	0.042	0.90	18.6%
5	11	40	1.0	3.1	1.18	1.1	4	3.2	0.31	0.0118	0.575	0.436	0.57	0.072	0.88	22.9%
6	11	40	2.0	3.5	0.52	1.1	4	6.3	0.35	0.0052	0.675	0.555	0.22	0.053	0.94	12.5%
7	16	40	2.0	3.8	0.38	1.6	4	6.3	0.38	0.0038	1.031	1.047	0.17	0.042	0.95	10.1%
8	11	40	2.0	3.7	0.37	1.1	4	6.3	0.37	0.0037	0.512	0.367	0.15	0.036	0.95	9.6%
9	16	40	1.4	3.2	0.62	1.6	4	4.5	0.32	0.0062	0.823	0.747	0.33	0.062	0.93	13.8%
10	11	40	1.4	3.2	0.71	1.1	4	4.5	0.32	0.0071	0.713	0.602	0.31	0.057	0.92	15.4%
11	11	40	1.0	3.6	1.04	1.1	4	3.2	0.36	0.0104	0.986	0.979	0.50	0.066	0.87	23.5%
12	6	30	0.8	3.2	1.87	0.6	3	2.6	0.32	0.0187	1.536	1.904	0.41	0.043	0.81	33.7%
13	16	40	0.8	3.2	0.46	1.6	4	2.6	0.32	0.0046	0.633	0.504	0.55	0.050	0.95	10.4%
14	11	40	0.8	3.2	0.96	1.1	4	2.6	0.32	0.0096	0.632	0.502	0.53	0.051	0.89	19.9%

also the total horizontal force) was calculated using (18). Considering sheltering effects, the total horizontal force on one row of 30 aggregates of 10 sheltered blades was

$$F_{x,rms} = \sqrt{\frac{1}{T_w}\int_0^{T_w}\left[\frac{1}{2}nC_{di}\rho b l_r|U|U + \alpha_F\beta_n nQ(s=0)\right]^2 dt} \tag{38}$$

with $n = 30$, $\beta_n = 10$, and $\overline{\alpha_F} = 0.724$.

The numerically calculated $F_{x,rms}$ for a row of blades and k_D for the canopy are compared with the measurements on Fig. 9. The calculated $F_{x,rms}$ and k_D have shown a good agreement with the measured data with normalized root-mean square-errors (NRMSE) of 0.40 (Fig. 9a) and 0.23 (Fig. 9b), respectively. The numerical model overestimated $F_{x,rms}$ by 1% while underestimated k_D by 10% (calculated using the slope of the linear fitting line on Fig. 9), indicating that the constant hydrodynamic coefficients, mean α_F, and mean α_ϵ are appropriate to predict the total horizontal force and wave attenuation in this study.

The designed model kelp canopy can reduce up to 33.7% of the wave energy when the canopy occupied a larger portion of the water column ($l/h = 0.34$), was located at higher position ($d_1/h = 0.20$), covered more wavelengths ($L_v/\lambda = 3.7$) and featured larger amplitude waves ($H_{I0}/h = 0.11$) as shown in Table 3.

The measured wave energy dissipation ratio (EDR) for the suspended model kelp canopy in different wave conditions and with different canopy vertical positions are shown on Fig. 10 as a function of the dimensionless parameters, λ/h, H_{I0}/h, l/h, and d_1/h. The numerically calculated EDR using (29) is also shown on Fig. 10 to help analyze the trend of EDR. It is noted that EDR first increases with λ/h and then decreases with λ/h (Fig. 10a) showing a different behavior from submerged canopies, of which the wave attenuation capacity increases with wavelength (e.g., Fig. 6c in Luhar et al., 2017). The EDR is not sensitive to H_{I0}/h. For example on Fig. 10b, EDR increases a little by 3% from 0.150 to 0.154 when H_{I0}/h increases dramatically by 77% from 0.046 to 0.081. The EDR increases with l_f/h (Fig. 10c). As the water depth decreases, the canopy occupies more of the water column so that EDR increases. The results also demonstrate that moving the canopy upward (reducing d_1/h) can improve the wave attenuation (Fig. 10d) as expected.

4.4. Bulk drag coefficient and effective blade length

For convenience in implementing the wave attenuation model into large scale models and to improve computational efficiency, empirical formulas for the bulk drag coefficient and the effective blade length of the suspended canopy for wave attenuation were developed based on the datasets. For the blade with rigid part (l_r) and flexible part (l_f), the wave decay coefficient k_D can be split into two parts as $k_D = k_{Dr} + k_{Df}$ with k_{Dr} for the rigid part and k_{Df} for the flexible part of the blade. The k_{Dr} for the rigid part is calculated using (25) with $l = l_r$ and C_{di} calculated using (14). The measured k_{Df} is obtained by subtracting k_{Dr} from the measured k_D. With measured k_{Df}, the bulk drag coefficient ($C_{DB,f}$) for the flexible part of the blade is solved from (26), and the effective blade length ($l_{f,e}$) is solved from (27) with C_{di} calculated using (14). The calculated C_{di} are shown in Table 1.

For unsteady flow, $C_{DB,f}$ is better fitted as a function of KC than Re. The fitted relation between $C_{DB,f}$ and KC for the suspended model kelp canopy is

$$C_{DB,f} = (3.6 \pm 0.7)KC^{-1.02\pm0.10}, \tag{39}$$

with $R^2 = 0.92$ (Fig. 11a). With the bulk drag coefficient $C_{DB,f}$, the wave decay coefficient k_{Df} for the flexible part can therefore be calculated directly using (26) without calculating the blade motion.

Based on the scaling analysis with linear blade motion, Luhar and Nepf (2016) argued that $l_{f,e}$ is proportional to $(CaL)^{-0.25}$. Following Luhar and Nepf (2016), the best fit for $l_{f,e}$ is

$$\frac{l_{f,e}}{l_f} = (1.11 \pm 0.08)(CaL)^{-0.25}, \tag{40}$$

with $R^2 = 0.06$ (Fig. 11b). With the effective blade length $l_{f,e}$, the wave decay coefficient k_{Df} for the flexible part can therefore be calculated directly using (27) with C_{di} in (14) without calculating the blade motion.

To evaluate the performance of the fitted formulas for $C_{DB,f}$ and $l_{f,e}$, the calculated k_{Df} using (26) with fitted $C_{DB,f}$ in (39) and using (27) with fitted $l_{f,e}$ in (40) are compared with the measured k_{Df} as well as the numerically calculated k_{Df} using (24) as shown on Fig. 11c. The NRMSE for the calculated k_{Df} with fitted $C_{DB,f}$ is 0.08, which is smaller than the calculations with fitted $l_{f,e}$ (NRMSE = 0.13). The improved performance of the bulk drag coefficient method is due to the better fit for $C_{DB,f}$ as a function of KC with a larger $R^2 = 0.92$ than the effective blade length method ($R^2 = 0.06$), which fits $l_{f,e}$ as a function of CaL. Both the bulk drag coefficient and the effective blade length methods have shown a smaller NRMSE than that of the numerical calculations without fitting (NRMSE = 0.27). This indicates that the simplified methods using the bulk drag coefficient and effective blade length that are fitted with experiments are successful for considering the influences of blade motion on wave attenuation. In fact, they performed even better than the numerical methods (24) that resolves the blade motion. This is because the values of $C_{DB,f}$ and $l_{f,e}$ are derived from empirical fits to the data that they are used to predict. Additionally, the fitted values incorporated all the uncertainties, such as

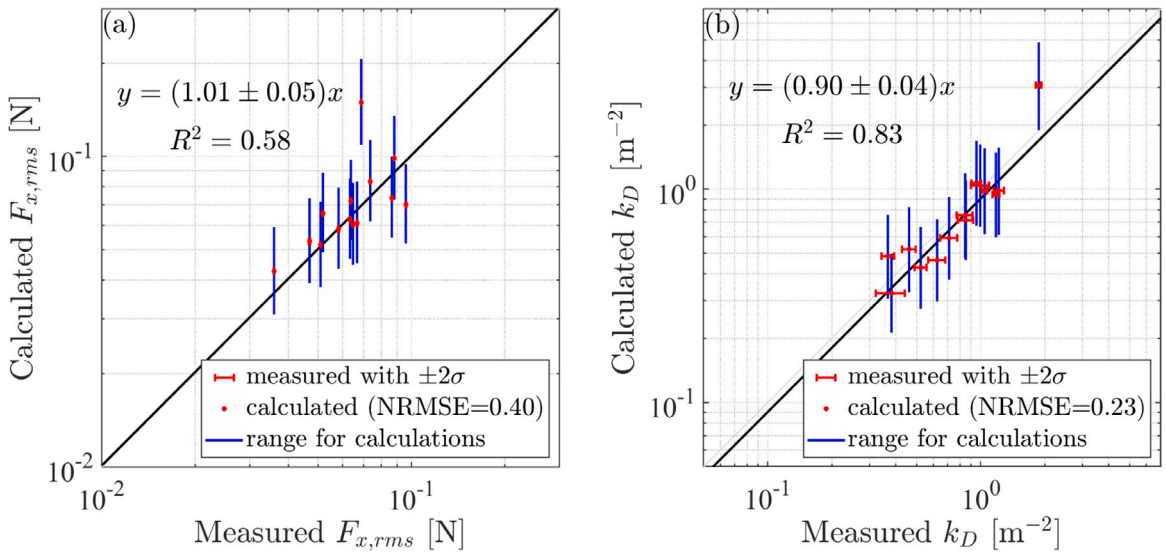

Fig. 9. Comparisons for the measured and calculated (a) horizontal force ($F_{x,rms}$) for a row of 30 aggregates of 10 sheltered blades and (b) wave decay coefficient (k_D). The vertical error bars indicate two standard deviations (2σ) for the measurements while the horizontal bars indicate the computation uncertainty induced by using the minimum and maximum force ratio α_F and sheltering factor α_c. The normalized root mean square error (NRMSE) for the calculated values is shown in the legend. The black lines are the linear fit for the calculated $F_{x,rms}$ and k_D with expressions and R^2 nearby.

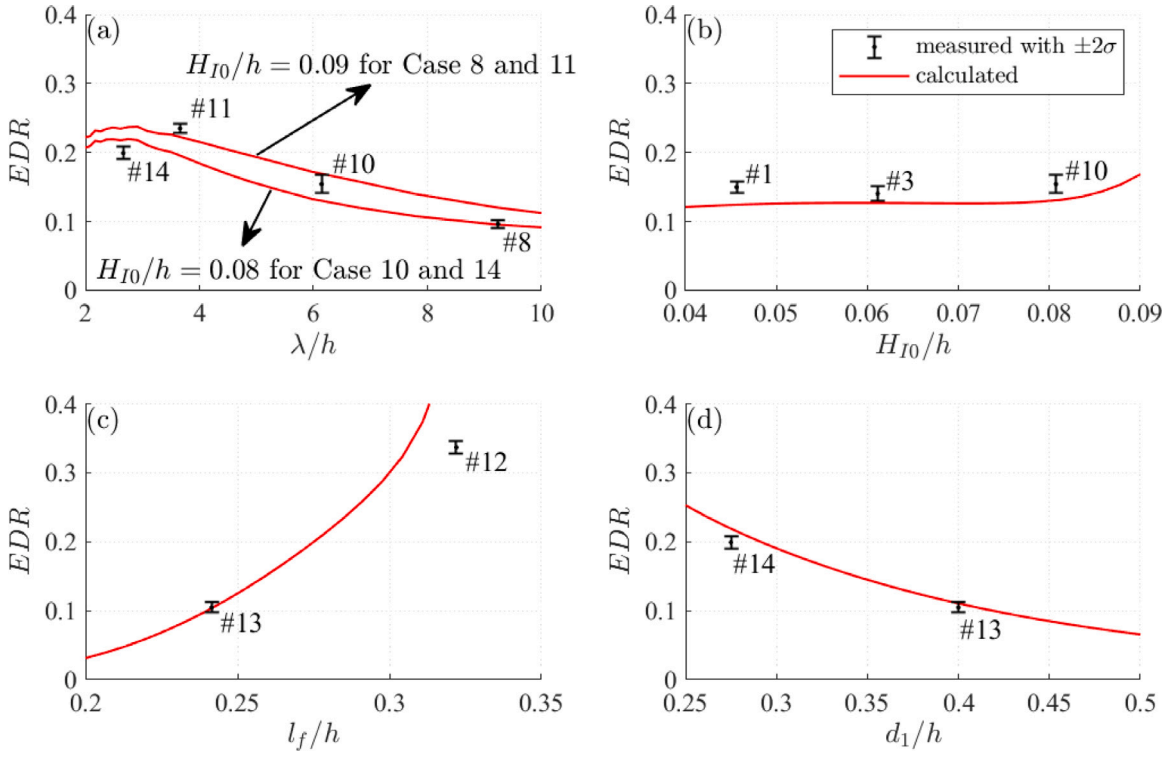

Fig. 10. Measured and calculated wave energy dissipation ratio (EDR) for the suspended model kelp canopy as a function of (a) λ/h, (b) H_{I0}/h, (c) l/h, and (d) d_1/h. The water depth is h, the wavelength is λ, the incident wave height is H_{I0}, the blade length is l, and the vertical distance from the longline to the still water line is d_1. The measured EDR is denoted by black crosses with the corresponding case numbers nearby while the calculated EDR using the averaged sheltering factor is denoted by red lines. In (a), the upper red line indicates the calculations for Case 8 and 11 with $H_{I0}/h = 0.09$ while the lower red line indicates the calculations for Case 10 and 14 with $H_{I0}/h = 0.08$. They are presented together in (a) since their H_{I0}/h are close and have no significant influences on EDR.

the velocity reduction in the canopy (Lowe, 2005), that the numerical methods did not consider.

5. Discussion

The blade roll-over phenomenon is expected to influence wave attenuation, therefore, understanding the wave induced dynamics is important to assess if this is anticipated in the field. Additionally, it is critical to analyze if simplified methods (i.e. the bulk drag coefficient and effective blade length) can be used to enhance computational efficiency in wave attenuation simulations. Before kelp farms can be implemented as nature-based coastal protection measures, it is essential to identify the key parameters affecting wave attention.

5.1. Roll-over of suspended flexible blades

The suspended blade fixed at the upper end exhibited different dynamics compared to the submerged blade fixed at the sea floor. The

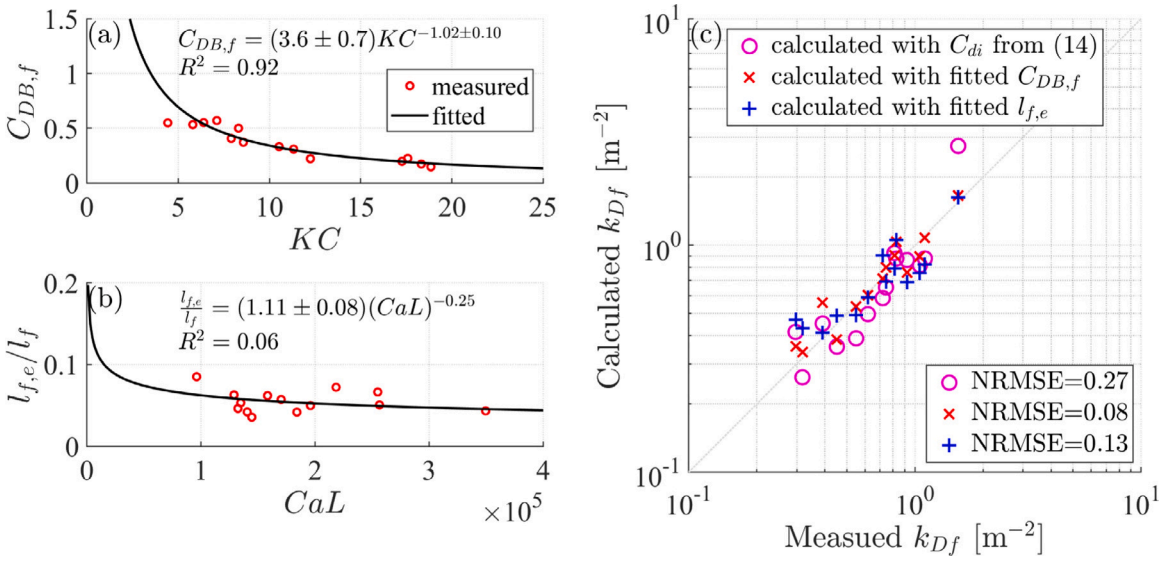

Fig. 11. (a) Measured bulk drag coefficients ($C_{DB,f}$) for the flexible part of the blade as a function of Keulegan–Carpenter number (KC). (b) Measured effective blade length ($l_{f,e}$) for the flexible part (l_f) of the blade as a function of the product of Cauchy number (Ca) and length ratio (L). In (a) and (b), the black line indicates the fitting formula with expression and R^2 nearby. (c) Comparisons between the measured wave decay coefficient k_{Df} for the flexible part of the blade and the calculations using (24) with C_{di} calculated from (14) (denoted by magenta open circles), using (26) with fitted $C_{DB,f}$ (denoted by red ×), and using (27) with fitted $l_{f,e}$ (denoted by blue +). The normalized root mean square error (NRMSE) is shown in the legend.

differences are represented by the opposite asymmetric motion and roll-over property of the suspended blade. The opposite asymmetric motion of suspended blades is mainly induced by the asymmetric action of the vertical wave orbital velocity. In waves propagating to the right as an example, the wave orbital motion provides a clockwise momentum that drives bottom-fixed blade to incline to the right while drives top-fixed blades to incline to the left. Similarly, the rolling over motion of the suspended blades also results from the interaction of the blade with wave orbital motion. The blade motion is driven by the wave orbital motion. For a long flexible blade in transitional and deep water waves, the blade motion is asymmetric (Zhu et al., 2020b). When the wave height increases to a critical value, the asymmetry becomes so large that the blade is almost horizontal, providing conditions for the onset of rolling over.

For aquaculture farms, the blades are closely seeded as an aggregate. The sheltering effects and blade–blade interaction may inhibit the rolling over cycle by cycle. In the experiments, only waves were considered. In the field, the strong background currents can streamline the blade and therefore inhibit rolling over. However, the rolling over can still happen for sparsely seeded kelp in large wave conditions. The blade roll-over induces a large curvature resulting in a large inner stress that increases the risk of blade breakage. Long-term roll-over is expected to also impact kelp growth and morphology. The blade roll-over reduces canopy height and increase blade–blade sheltering and interaction, which may decrease wave attenuation. However, the roll-over effects may reduce the blade motion amplitude and move the lower part of the blade upward that may enhance wave attenuation. The roll-over effects are still unclear that warrant further investigation in the future.

5.2. Methods to predict wave attenuation

The aquaculture kelp blades are seeded closely together on the long-line for economic benefits. High plant density (e.g., 745/m in Peteiro and Freire, 2013) is also beneficial for wave attenuation. However, the sheltering effects from neighboring blades and the blade–blade interaction present uncertainties for wave attenuation prediction. A simple sheltering factor defined in (33) is acceptable since the numerical calculations with the sheltering factor present a small NRMSE of 0.23 (Fig. 9b). As the plant density and blade configurations influence the sheltering effects, a more sophisticated sheltering factor as a function of plant density and blade properties as well as wave conditions is warranted.

Compared to the numerical wave decay coefficient calculated with (24), the bulk drag coefficient and effective blade length methods have improved the calculations by reducing the NRMSE by 70% and 52%, respectively. The improvements are attributed to the fits for $C_{DB,f}$ and $l_{f,e}$ based on the data that are being predicted. The bulk drag coefficient and effective blade length methods are simple and convenient to implement into large-scale models. Although the bulk drag coefficient and effective blade length methods could provide favorable results with fitted C_{DB} and l_e, physical experiments are required to calibrate C_{DB} and l_e. Thus, the numerical solution (24) could be an alternative when reliable C_{DB} and l_e are not available.

5.3. Suspended kelp aquaculture farms as nature-based coastal protection

The model kelp canopy has shown the capacity for wave attenuation in the laboratory experiments. Though, this anticipated wave attenuation is overestimated because the model blade thickness is $d = d_{\max}$ as constant while the thickness of real kelp reduces towards the blade edge (Fig. 5c). Based on the thickness distribution in (36), the second momentum of the cross section of *S. latissima* is

$$I = \int_{-\frac{1}{2}d_{\max}}^{\frac{1}{2}d_{\max}} 2 \mid s_b \mid y^2 dy \approx \frac{0.2b\, d_{\max}^3}{12}, \tag{41}$$

indicating that the flexural rigidity of the real *S. latissima* blade is only 20% of the same wide plate but with the maximum thickness. To reduce the overestimation and obtain more reliable results for the wave attenuation in the field, an effective blade width $b_e = 0.2b$ is used in the following discussion. By removing the overestimation due to using maximum thickness, the wave energy dissipation ratio (EDR) drops from 10% to 1.5% (Fig. 12a) for Case 6 in Table 3. In addition, the bending elastic modulus (E) of the full scale model blade is designed as 21.0 MPa, which is near the largest measured E. The measured E ranges from 2.7 ± 1.4 to 22 ± 6 MPa (Table 2) and varies along the blade length (Fig. 2a). For the given blade thickness of 0.79 mm, the expected bending elastic modulus is E = 5.6 MPa based on (37).

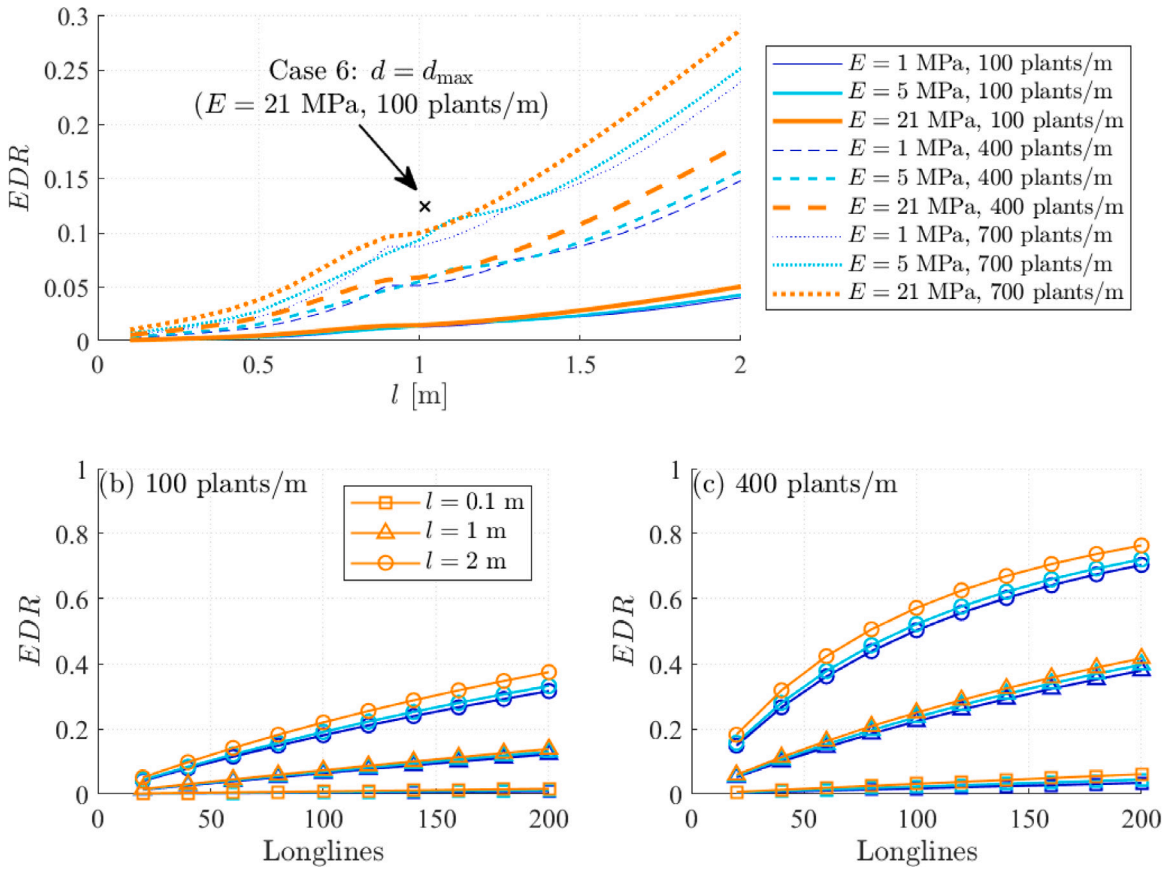

Fig. 12. (a) Effects of the bending elastic modulus (E) and the length (l) of the blade as well as number of plants per meter on the wave energy dissipation ratio (EDR) of suspended kelp aquaculture farms. Wave attenuation as a function of the number of kelp longlines with (b) 100 plants/m and (c) 400 plants/m with $l = 0.1$ (square), 1 (triangle), 2 (circle) m and $E = 1$ (blue), 5 (cyan), 21 (orange) MPa. The water depth is 4 m, wave height is 0.35 m, and wave period is 6.3 s. The kelp longline is 1.1 m beneath the still water line. The blade thickness is d and the maximum thickness is $d_{\max}$. (For interpretation of the references to color in this figure legend, the reader is referred to the web version of this article.)

However, the numerical results show that E has a small influence on wave attenuation (Fig. 12). For example in Case 6, the EDR reduces from 1.5% to 1.4% by 6.7% when E decreases from 21 MPa to 5 MPa by 76% (Fig. 12a).

The plant density is 100 plants/m for the model kelp longline, which is smaller than the measured value of 405 plants/m. In fact, the plant density can be as large as 745 plants/m (Peteiro and Freire, 2013), which can significantly enhance the wave attenuation. Assuming the measured sheltering factor α_ϵ is applicable for larger plant density, the simulated EDR for Case 6 increases to 5.5% with 400 plants/m and to 9.4% with 700 plants/m with effective blade width $b_e = 0.2b$ and $E = 5$ MPa (Fig. 12a). As the growth of kelp, the blade length increases yielding larger wave attenuation. For instance with 400 plants/m and $E = 5$ MPa, the EDR increases from 5.5% to 15.7% when the blade length grows from 1 m to 2 m. The increase of EDR is even more significant (25.2%) for a greater plant density of 700 plants/m.

The wave attenuation of suspended aquaculture kelp is dependent on the growth of kelp including the blade size and plant density, where a denser longline with longer kelp yields more wave attenuation. Another important parameter determining the wave attenuation of a suspended kelp farm is the number of longlines. For the suspended kelp farm with 200 longlines with 100 plants/m in the same conditions with Case 6, the EDR are 13.0% for 1 m-long blades with $E = 5$ MPa and 33.2% for 2 m-long blades with $E = 5$ MPa (Fig. 12b). If the plant density increases to 400 plants/m as measured in this study, the EDR increase to 40.0% and 72.1% (Fig. 12c), respectively. The vertical position of kelp in the water column also influences the wave attenuation. Generally, the higher location in the water column results in larger wave attenuation. However, the vertical position also influences the growth of kelp due to the depth distribution of light, temperature, and nutrient (Graham et al., 2007; Bekkby et al., 2019), which should be considered in the application of suspended kelp aquaculture farms for wave attenuation.

The wave attenuation capacity of suspended kelp aquaculture farms is also dependent on the wave conditions, especially the water depth and wavelength. Although (29) shows that EDR is dependent on $k_D H_0$, EDR is not certainly significantly influenced by H_0. Noted that $k_D H_0 \propto C_{DB} H_0 \propto KC^{-1.02} H_0 \propto U_m^{-1.02} H_0 \propto H_0^{-1.02} H_0 = H_0^{-0.02} \approx 1$ based on the bulk drag coefficient method with k_D in (26), C_{DB} in (39), KC in (9), and U in (19). Therefore, the wave attenuation is not sensitive to the incident wave height, which is also demonstrated in the experiments as shown on Fig. 10b. However, the wave attenuation can be improved significantly by locating the suspended kelp farms in shallower water such that the kelp blade occupies a larger fraction of the water column, especially for shallow water waves. In shallow water waves ($kh < 0.1\pi$), the wave decay coefficient k_D in (26) is reduced to

$$k_D = \frac{\alpha_\epsilon C_{DB} b N l}{3\pi h^2}, \tag{42}$$

indicating that k_D increases quadratically with decreasing water depth in shallow water waves. The water depth is also an important factor for kelp growth. Furthermore, the wave attenuation of suspended kelp farms increases with wavelength and then decreases with wavelength, indicating that the suspended kelp farms do not perform well for very short waves and very long waves. This is because in very short waves, the wave kinematic energy concentrates on the water particles above

the kelp canopy and in very long waves, the canopy length covers few wavelength.

Overall, the wave attenuation effectiveness of suspended kelp farms can be improved by installing the kelp farms in shallower water, expanding the farm size by adding more longlines, and locating the kelp in a higher position of the water column. Choosing the kelp species with more rigid, wider, and longer blades/biomass and growing the kelp more densely can further improve the wave attenuation.

5.4. Limitations

This preliminary study has proposed simple methods to quantify the wave attenuation of suspended kelp aquaculture structures. However, there are still some limitations of these methods due to the complexity of the kelp morphology and flow environment in the field. The kelp blade morphology is more flat in exposed sites and more ruffled in sheltered sites (Koehl et al., 2008). The ruffle and thickness variance of the blade may impact the hydrodynamic coefficients. Like kelp stipe and holdfast, these small morphological features cannot be fully considered in the downscaled model and the effects of these small morphological features on wave attenuation are unclear. In the field, there would be a background current in addition to waves that may have significant influences on the wave attenuation, which is not considered in the current study. When the current exceeds a critical value, the kelp becomes streamlined so that the drag force decreases and the friction dominates (Fredriksson et al., 2020), after which a smaller wave attenuation is anticipated. At this point, the energy conservation equation (21) should be modified by using friction rather than the normal drag. Gaylord et al. (2003) observed that the alongshore currents decrease the wave attenuation of *Nereocystis luetkeana*. However, the reconfiguration of kelp in waves and currents can enhance the survival rate and reduce the effects of wave attenuation service on the biomass productivity (Gerard, 1987). Lastly, the kelp longline mooring system and the motion of the longline were not considered due to the small width of the flume, which may lead to overestimation of the wave attenuation.

6. Conclusions

Wave attenuation by suspended kelp canopies was investigated using a set of physical model experiments having dynamic similarity with cultivated *S. latissima* from an aquaculture site in Saco Bay, Maine of the USA. The yield of the kelp farm was 6.86 kg/m with 405 plants/m. The cultivated *S. latissima* had a length of 3–177.7 cm, width of 1–18.5 cm, thickness of 0.44–1.08 mm, mass density of 1.05 g/cm^3, and elastic modulus of 2.7–22 MPa. The model kelp farm was configured to have 20 grow lines of 1-m-long blades and 100 blades/m with an orientation normal to the direction of waves. The experimental results demonstrated that in this configuration, a suspended kelp farm could attenuate wave energy by 16.3%, 18.6%, 23.5%, and 33.7% for 6.3 s, 4.5 s, 3.2 s, and 2.6 s waves, respectively, in water depth of 3–4 m. The physical model results also showed that the motion of suspended blades was asymmetric, similar to bottom-fixed blades, but yielded a blade inclination that opposed the direction of wave propagation. In waves propagating to the right, the clockwise motion of water particles induces a clockwise momentum that drives the blades to bend clockwise around the fixed end. As suspended blades are fixed at the top end, the clockwise bending of suspended blades results in an inclination to the left. In contrast, the bottom-fixed blade inclines to the right. In large waves, this strong asymmetric motion promoted a roll over motion of the suspended blades.

To predict wave attenuation under a wider range of conditions and to identify the key parameters affecting wave attenuation, a numerical model was developed that could resolve blade motion. The numerical model showed good agreement with the experiments with a slight underestimation of 10%. The results indicate that (i) the wave energy dissipation ratio (EDR) of suspended kelp farms decreases with increased water depth, (ii) EDR is not sensitive to wave height, (iii) EDR first increases and then decreases with wavelength, and (iv) EDR increases with blade size, kelp vertical position, plant density, and the number of longlines. Therefore, the technique to improve the wave attenuation capacity of suspended kelp aquaculture farms for nature-based coastal defense is to install the kelp farms in shallower water, expand the farm size by adding more longlines, locate the kelp in a higher position of the water column, grow the kelp more densely, and choose the kelp species with more rigid, wider, and longer blades/biomass.

The results of this study also produced empirical formulas for the bulk drag coefficient and effective blade length of suspended kelp canopy for wave attenuation applications. These expressions could be implemented in large-scale wave models to examine the role of kelp farms as nature-based coastal protection measures on coastal morphology, inner shelf circulation and material transport. Though this study focused on waves without currents, a natural extension of this work would be to include background currents, which likely streamline the kelp blades and influence the wave attenuation performance.

CRediT authorship contribution statement

Longhuan Zhu: Conceptualization, Methodology, Software, Validation, Formal analysis, Investigation, Resources, Data curation, Writing – original draft, Writing - review & editing, Visualization. **Jiarui Lei:** Methodology, Writing - review & editing. **Kimberly Huguenard:** Supervision, Resources, Writing - review and editing. **David W. Fredriksson:** Resources, Writing - review & editing.

Declaration of competing interest

The authors declare that they have no known competing financial interests or personal relationships that could have appeared to influence the work reported in this paper.

Acknowledgments

This work was completed as part of the PhD research of Longhuan Zhu who was supported by National Science Foundation, USA award #IIA-1355457 to Maine EPSCoR at the University of Maine. The authors gratefully acknowledge the assistance of the Advanced Computing Group of the University of Maine System in producing the numerical data. Longhuan Zhu would like to sincerely thank Heidi Nepf for supporting the experiments and discussions at MIT, Neil Fisher and Allen Treadwell for assisting designing and manufacturing the kelp supporting frames, Adam St. Gelais and Kathryn Johndrow for assisting collecting *S. latissima* samples from the kelp longline of the University of New England, Kathryn Johndrow for measuring the blade length and width of kelp samples. Longhuan Zhu would also like to thank Yu-Ying Chen for assisting to measure the morphological and mechanical properties of *S. latissima* and his colleagues in the coastal research group of the University of Maine and friends for help in preparing model kelp longlines. All data generated or analyzed during this study are included in this manuscript. The raw data are available from the authors upon reasonable request. Finally, the authors would like to thank the anonymous reviewer for constructive comments that really helped to improve this manuscript greatly.

Appendix A. Wave height fitting along a canopy with reflective waves

Assuming the incident wave height (H_{I0}) and reflective wave height (H_{RL_v}) decay at the same decay coefficient k_D following (23), the

$$\begin{aligned}\eta &= \eta_I + \eta_R \\ &= \frac{1}{2}\left[\frac{H_{I0}}{1+k_D H_{I0}x}\cos(kx+\epsilon_I) + \frac{H_{RL_v}}{1+k_D H_{RL_v}(L_v-x)}\cos(kx+\epsilon_R)\right]\cos(\omega t) \\ &+ \frac{1}{2}\left[\frac{H_{I0}}{1+k_D H_{I0}x}\sin(kx+\epsilon_I) - \frac{H_{RL_v}}{1+k_D H_{RL_v}(L_v-x)}\sin(kx+\epsilon_R)\right]\sin(\omega t) \\ &= \frac{1}{2}\sqrt{\left(\frac{H_{I0}}{1+k_D H_{I0}x}\right)^2 + \left[\frac{H_{RL_v}}{1+k_D H_{RL_v}(L_v-x)}\right]^2 + 2\frac{H_{I0}}{1+k_D H_{I0}x}\frac{H_{RL_v}}{1+k_D H_{RL_v}(L_v-x)}\cos(2kx+\epsilon)} \\ &\cdot \cos(\omega t+\psi),\end{aligned} \tag{A.3}$$

Box II.

$$H(x) = \sqrt{\left(\frac{H_{I0}}{1+k_D H_{I0}x}\right)^2 + \left[\frac{H_{RL_v}}{1+k_D H_{RL_v}(L_v-x)}\right]^2 + 2\frac{H_{I0}}{1+k_D H_{I0}x}\frac{H_{RL_v}}{1+k_D H_{RL_v}(L_v-x)}\cos(2kx+\epsilon)}. \tag{A.4}$$

Box III.

incident water elevation (η_I) and reflective water elevation (η_R) can be expressed as

$$\eta_I = \frac{H_{I0}}{2}\frac{1}{1+k_D H_{I0}x}\cos(kx-\omega t+\epsilon_I) \tag{A.1}$$

and

$$\eta_R = \frac{H_{RL_v}}{2}\frac{1}{1+k_D H_{RL_v}(L_v-x)}\cos(kx+\omega t+\epsilon_R), \tag{A.2}$$

respectively, where ϵ_I and ϵ_R are the incident wave phase and reflective wave phase, respectively. Therefore, the combined water elevation η can be expressed as (A.3) in Box II, where $\epsilon = \epsilon_I + \epsilon_R$, and $\psi = -\frac{H_{I0}[1+k_D H_{RL_v}(L_v-x)]\sin(kx+\epsilon_I)-H_{RL_v}(1+k_D H_{I0}x)\sin(kx+\epsilon_R)}{H_{I0}[1+k_D H_{RL_v}(L_v-x)]\cos(kx+\epsilon_I)+H_{RL_v}(1+k_D H_{I0}x)\cos(kx+\epsilon_R)}$. Thus, the wave height along the canopy can be obtained and given by (A.4) in Box III.

Appendix B. Supplementary data

Supplementary material related to this article can be found online at https://doi.org/10.1016/j.coastaleng.2021.103947.

References

Abdelrhman, M., 2007. Modeling coupling between eelgrass zostera marina and water flow. Mar. Ecol. Prog. Ser. 338, 81–96. http://dx.doi.org/10.3354/meps338081, URL: http://www.int-res.com/abstracts/meps/v338/p81-96/.

Anderson, M.E., Smith, J., 2014. Wave attenuation by flexible, idealized salt marsh vegetation. Coast. Eng. 83, 82–92. http://dx.doi.org/10.1016/j.coastaleng.2013.10.004, URL: https://linkinghub.elsevier.com/retrieve/pii/S0378383913001609.

Asano, T., Deguchi, H., Kobayashi, N., 1992. Interaction between water waves and vegetation. In: Coastal Engineering Proceedings, Vol. 3. pp. 2710–2723, URL: https://icce-ojs-tamu.tdl.org/icce/index.php/icce/article/view/4885.

Augustin, L.N., Irish, J.L., Lynett, P., 2009. Laboratory and numerical studies of wave damping by emergent and near-emergent wetland vegetation. Coast. Eng. 56 (3), 332–340. http://dx.doi.org/10.1016/j.coastaleng.2008.09.004, URL: https://linkinghub.elsevier.com/retrieve/pii/S037838390800152X.

Augyte, S., Yarish, C., Redmond, S., Kim, J.K., 2017. Cultivation of a morphologically distinct strain of the sugar kelp, saccharina latissima forma angustissima, from coastal maine, USA, with implications for ecosystem services. J. Appl. Phycol. 29 (4), 1967–1976. http://dx.doi.org/10.1007/s10811-017-1102-x, URL: http://link.springer.com/10.1007/s10811-017-1102-x.

Bekkby, T., Smit, C., Gundersen, H., Rinde, E., Steen, H., Tveiten, L., Gitmark, J.K., Fredriksen, S., Albretsen, J., Christie, H., 2019. The abundance of kelp is modified by the combined impact of depth, waves and currents. Front. Mar. Sci. 6 (JUL), 475. http://dx.doi.org/10.3389/fmars.2019.00475, URL: https://www.frontiersin.org/article/10.3389/fmars.2019.00475/full.

Bradley, K., Houser, C., 2009. Relative velocity of seagrass blades: Implications for wave attenuation in low-energy environments. J. Geophys. Res. 114 (F1), F01004. http://dx.doi.org/10.1029/2007JF000951, URL: http://doi.wiley.com/10.1029/2007JF000951.

Breton, T.S., Nettleton, J.C., O'Connell, B., Bertocci, M., 2018. Fine-scale population genetic structure of sugar kelp, saccharina latissima (laminariales, phaeophyceae), in eastern maine, USA. Phycologia 57 (1), 32–40. http://dx.doi.org/10.2216/17-72.1, URL: https://www.tandfonline.com/doi/full/10.2216/17-72.1.

Bricknell, I.R., Birkel, S.D., Brawley, S.H., Van Kirk, T., Hamlin, H., Capistrant-Fossa, K., Huguenard, K., Van Walsum, G.P., Liu, Z.L., Zhu, L.H., Grebe, G., Taccardi, E., Miller, M., Preziosi, B.M., Duffy, K., Byron, C.J., Quigley, C.T., Bowden, T.J., Brady, D., Beal, B.F., Sappati, P.K., Johnson, T.R., Moeykens, S., 2020. Resilience of cold water aquaculture: a review of likely scenarios as climate changes in the gulf of maine. Rev. Aquac. raq.12483. http://dx.doi.org/10.1111/raq.12483, URL: https://onlinelibrary.wiley.com/doi/abs/10.1111/raq.12483.

Buck, B.H., Buchholz, C.M., 2005. Response of offshore cultivated laminaria saccharina to hydrodynamic forcing in the north sea. Aquaculture 250 (3–4), 674–691. http://dx.doi.org/10.1016/j.aquaculture.2005.04.062, URL: https://linkinghub.elsevier.com/retrieve/pii/S0044848605003248.

Campbell, I., Macleod, A., Sahlmann, C., Neves, L., Funderud, J., Øverland, M., Hughes, A.D., Stanley, M., 2019. The environmental risks associated with the development of seaweed farming in europe - prioritizing key knowledge gaps. Front. Mar. Sci. 6 (MAR), 107. http://dx.doi.org/10.3389/fmars.2019.00107, URL: https://www.frontiersin.org/article/10.3389/fmars.2019.00107/full.

Chen, H., Liu, X., Zou, Q., 2019. Wave-driven flow induced by suspended and submerged canopies. Adv. Water Resour. 123, 160–172. http://dx.doi.org/10.1016/j.advwatres.2018.11.009, URL: https://linkinghub.elsevier.com/retrieve/pii/S0309170818302574.

Chen, H., Ni, Y., Li, Y., Liu, F., Ou, S., Su, M., Peng, Y., Hu, Z., Uijttewaal, W., Suzuki, T., 2018. Deriving vegetation drag coefficients in combined wave-current flows by calibration and direct measurement methods. Adv. Water Resour. 122, 217–227. http://dx.doi.org/10.1016/j.advwatres.2018.10.008, URL: https://linkinghub.elsevier.com/retrieve/pii/S030917081830112X.

Chen, Q., Zhao, H., 2012. Theoretical models for wave energy dissipation caused by vegetation. J. Eng. Mech. 138 (2), 221–229. http://dx.doi.org/10.1061/(ASCE)EM.1943-7889.0000318, URL: http://ascelibrary.org/doi/10.1061/%28ASCE%29EM.1943-7889.0000318.

Chen, H., Zou, Q.-P., 2019. EulerIan–Lagrangian flow-vegetation interaction model using immersed boundary method and openfoam. Adv. Water Resour. 126, 176–192. http://dx.doi.org/10.1016/j.advwatres.2019.02.006, URL: https://linkinghub.elsevier.com/retrieve/pii/S0309170818306523.

Dalrymple, R.A., Kirby, J.T., Hwang, P.A., 1984. Wave diffraction due to areas of energy dissipation. J. Waterw. Port Coast. Ocean Eng. 110 (1), 67–79. http://dx.doi.org/10.1061/(ASCE)0733-950X(1984)110:1(67), URL: http://ascelibrary.org/doi/10.1061/%28ASCE%290733-950X%281984%29110%3A1%2867%29.

Dean, R.G., Dalrymple, R.A., 1991. Water Wave Mechanics for Engineers and Scientists. In: Advanced Series on Ocean Engineering, vol. 2, WORLD SCIENTIFIC, Cambridge, http://dx.doi.org/10.1142/1232.

Duarte, C.M., Wu, J., Xiao, X., Bruhn, A., Krause-Jensen, D., 2017. Can seaweed farming play a role in climate change mitigation and adaptation?. Front. Mar. Sci. 4 (APR), 100. http://dx.doi.org/10.3389/fmars.2017.00100, URL: http://journal.frontiersin.org/article/10.3389/fmars.2017.00100/full.

Elwany, M.H.S., O'Reilly, W.C., Guza, R.T., Flick, R.E., 1995. Effects of southern california kelp beds on waves. J. Waterw. Port Coast. Ocean Eng. 121 (2), 143–150. http://dx.doi.org/10.1061/(ASCE)0733-950X(1995)121:2(143), URL: http://ascelibrary.org/doi/10.1061/%28ASCE%29WW.1943-5460.0000251.

Fredriksson, D.W., Dewhurst, T., Drach, A., Beaver, W., St. Gelais, A.T., Johndrow, K., Costa-Pierce, B.A., 2020. Hydrodynamic characteristics of a full-scale kelp model for aquaculture applications. Aquac. Eng. 90, 102086. http://dx.doi.org/10.1016/j.aquaeng.2020.102086.

Fryer, M., Terwagne, D., Reis, P.M., Nepf, H., 2015. Fabrication of flexible blade models from a silicone-based polymer to test the effect of surface corrugations on drag and blade motion. Limnol. Oceanogr.: Methods 13 (11), 630–639. http://dx.doi.org/10.1002/lom3.10053, URL: http://doi.wiley.com/10.1002/lom3.10053.

Gaylord, B.P., Denny, M.W., Koehl, M.A., 2003. Modulation of wave forces on kelp canopies by alongshore currents. Limnol. Oceanogr. 48 (2), 860–871. http://dx.doi.org/10.4319/lo.2003.48.2.0860, URL: https://aslopubs.onlinelibrary.wiley.com/doi/pdf/10.4319/lo.2003.48.2.0860.

Gaylord, B., Rosman, J.H., Reed, D.C., Koseff, J.R., Fram, J., Macintyre, S., Arkema, K.K., Mcdonald, C., Brzezinski, M.A., Largier, J.L., Monismith, S.G., Raimondi, P.T., Mardian, B., 2007. Spatial patterns of flow and their modification within and around a giant kelp forest. Limnol. Oceanogr. 52 (5), 1838–1852, URL: https://aslopubs.onlinelibrary.wiley.com/doi/pdf/10.4319/lo.2007.52.5.1838.

Gerard, V.A., 1987. Hydrodynamic streamlining of laminaria saccharina lamour. in response to mechanical stress. J. Exp. Mar. Biol. Ecol. 107 (3), 237–244. http://dx.doi.org/10.1016/0022-0981(87)90040-2, URL: https://linkinghub.elsevier.com/retrieve/pii/0022098187900402.

Graham, M.H., Kinlan, B.P., Druehl, L.D., Garske, L.E., Banks, S., 2007. Deep-water kelp refugia as potential hotspots of tropical marine diversity and productivity. Proc. Natl. Acad. Sci. 104 (42), 16576–16580. http://dx.doi.org/10.1073/pnas.0704778104, URL: http://www.pnas.org/cgi/doi/10.1073/pnas.0704778104.

Grebe, G.S., Byron, C.J., Brady, D.C., Geisser, A.H., Brennan, K.D., 2021. The nitrogen bioextraction potential of nearshore saccharina latissima cultivation and harvest in the western gulf of maine. J. Appl. Phycol. 1–17. http://dx.doi.org/10.1007/s10811-021-02367-6, URL: http://link.springer.com/10.1007/s10811-021-02367-6.

Grebe, G.S., Byron, C.J., Gelais, A.S., Kotowicz, D.M., Olson, T.K., 2019. An ecosystem approach to kelp aquaculture in the americas and europe. Aquac. Rep. 15, 100215. http://dx.doi.org/10.1016/j.aqrep.2019.100215, URL: https://linkinghub.elsevier.com/retrieve/pii/S2352513419300134.

Henderson, S.M., 2019. Motion of buoyant, flexible aquatic vegetation under waves: Simple theoretical models and parameterization of wave dissipation. Coast. Eng. 152, 103497. http://dx.doi.org/10.1016/j.coastaleng.2019.04.009, URL: https://linkinghub.elsevier.com/retrieve/pii/S0378383918305349.

Hu, Z., Suzuki, T., Zitman, T., Uittewaal, W., Stive, M., 2014. Laboratory study on wave dissipation by vegetation in combined current–wave flow. Coast. Eng. 88, 131–142. http://dx.doi.org/10.1016/j.coastaleng.2014.02.009, URL: https://linkinghub.elsevier.com/retrieve/pii/S0378383914000416.

Huang, I., Rominger, J., Nepf, H., 2011. The motion of kelp blades and the surface renewal model. Limnol. Oceanogr. 56 (4), 1453–1462. http://dx.doi.org/10.4319/lo.2011.56.4.1453, URL: http://doi.wiley.com/10.4319/lo.2011.56.4.1453.

Jackson, G.A., 1984. Internal wave attenuation by coastal kelp stands. J. Phys. Oceanogr. 14 (8), 1300–1306. http://dx.doi.org/10.1175/1520-0485(1984)014<1300:IWABCK>2.0.CO;2, URL: http://journals.ametsoc.org/doi/abs/10.1175/1520-0485%281984%29014%3C1300%3AIWABCK%3E2.0.CO%3B2.

Jackson, G.A., 1997. Currents in the high drag environment of a coastal kelp stand off california. Cont. Shelf Res. 17 (15), 1913–1928. http://dx.doi.org/10.1016/S0278-4343(97)00054-X, URL: https://linkinghub.elsevier.com/retrieve/pii/S027843439700054X.

Jacobsen, N., McFall, B., van der A, D., 2019. A frequency distributed dissipation model for canopies. Coast. Eng. 150, 135–146. http://dx.doi.org/10.1016/j.coastaleng.2019.04.007, URL: https://linkinghub.elsevier.com/retrieve/pii/S0378383918303892.

Jadhav, R.S., Chen, Q., Smith, J.M., 2013. Spectral distribution of wave energy dissipation by salt marsh vegetation. Coast. Eng. 77, 99–107. http://dx.doi.org/10.1016/j.coastaleng.2013.02.013, URL: https://linkinghub.elsevier.com/retrieve/pii/S0378383913000537.

Keulegan, G.H., Carpenter, L.H., 1958. Forces on cylinders and plates in an oscillating fluid. J. Res. Natl. Bur. Stand. 60 (5), 423–440, URL: https://nvlpubs.nist.gov/nistpubs/jres/60/jresv60n5p423_A1b.pdf.

Kobayashi, N., Raichle, A.W., Asano, T., 1993. Wave attenuation by vegetation. J. Waterw. Port Coast. Ocean Eng. 119 (1), 30–48. http://dx.doi.org/10.1061/(ASCE)0733-950X(1993)119:1(30), URL: http://ascelibrary.org/doi/10.1061/%28ASCE%290733-950X%281993%29119%3A1%2830%29.

Koehl, M.A.R., Silk, W.K., Liang, H., Mahadevan, L., 2008. How kelp produce blade shapes suited to different flow regimes: A new wrinkle. Integr. Comp. Biol. 48 (6), 834–851. http://dx.doi.org/10.1093/icb/icn069, URL:https://academic.oup.com/icb/article-abstract/48/6/834/837623.

Lei, J., Nepf, H., 2019a. Blade dynamics in combined waves and current. J. Fluids Struct. 87, 137–149. http://dx.doi.org/10.1016/j.jfluidstructs.2019.03.020, URL: https://linkinghub.elsevier.com/retrieve/pii/S0889974618306996.

Lei, J., Nepf, H., 2019b. Wave damping by flexible vegetation: Connecting individual blade dynamics to the meadow scale. Coast. Eng. 147, 138–148. http://dx.doi.org/10.1016/j.coastaleng.2019.01.008, URL: https://linkinghub.elsevier.com/retrieve/pii/S0378383918300905.

Liang, B., Chaudet, P., Boisse, P., 2017. Curvature determination in the bending test of continuous fibre reinforcements. Strain 53 (1), 1–12. http://dx.doi.org/10.1111/str.12213, arXiv:NIHMS150003.

Losada, I.J., Maza, M., Lara, J.L., 2016. A new formulation for vegetation-induced damping under combined waves and currents. Coast. Eng. 107, 1–13. http://dx.doi.org/10.1016/j.coastaleng.2015.09.011, URL: https://linkinghub.elsevier.com/retrieve/pii/S0378383915001684.

Lowe, R.J., 2005. Oscillatory flow through submerged canopies: 1. Velocity structure. J. Geophys. Res. 110 (C10), C10016. http://dx.doi.org/10.1029/2004JC002788, URL: http://doi.wiley.com/10.1029/2004JC002788.

Luhar, M., 2012. Analytical and Experimental Studies of Plant-Flow Interaction at Multiple Scales (Thesis). Massachusetts Institute of Technology, URL: http://dspace.mit.edu/handle/1721.1/78142.

Luhar, M., Infantes, E., Nepf, H., 2017. Seagrass blade motion under waves and its impact on wave decay. J. Geophys. Res. Oceans 122 (5), 3736–3752. http://dx.doi.org/10.1002/2017JC012731, URL: http://doi.wiley.com/10.1002/2017JC012731.

Luhar, M., Nepf, H., 2016. Wave-induced dynamics of flexible blades. J. Fluids Struct. 61, 20–41. http://dx.doi.org/10.1016/j.jfluidstructs.2015.11.007, URL: arXiv:1510.01237.

Madsen, O.S., Poon, Y.-K., Graber, H.C., 1988. Spectral wave Attenuation by bottom friction: theory. Coast. Eng. Proc. 1 (21), 492–504. http://dx.doi.org/10.1061/9780872626874.035, URL: https://journals.tdl.org/icce/index.php/icce/article/view/4241.

Mao, X., Augyte, S., Huang, M., Hare, M.P., Bailey, D., Umanzor, S., Marty-Rivera, M., Robbins, K.R., Yarish, C., Lindell, S., Jannink, J.-L., 2020. Population genetics of sugar kelp throughout the northeastern united states using genome-wide markers. Front. Mar. Sci. 7, 694. http://dx.doi.org/10.3389/fmars.2020.00694, URL: https://www.frontiersin.org/article/10.3389/fmars.2020.00694/full.

Mendez, F.J., Losada, I.J., 2004. An empirical model to estimate the propagation of random breaking and nonbreaking waves over vegetation fields. Coast. Eng. 51 (2), 103–118. http://dx.doi.org/10.1016/j.coastaleng.2003.11.003, URL: https://linkinghub.elsevier.com/retrieve/pii/S0378383903001182.

Méndez, F.J., Losada, I.J., Losada, M.A., 1999. Hydrodynamics induced by wind waves in a vegetation field. J. Geophys. Res. 104 (C8), 18383–18396. http://dx.doi.org/10.1029/1999JC900119, URL: http://doi.wiley.com/10.1029/1999JC900119.

Mork, M., 1996. The effect of kelp in wave damping. Sarsia 80 (4), 323–327. http://dx.doi.org/10.1080/00364827.1996.10413607, URL: http://www.tandfonline.com/doi/full/10.1080/00364827.1996.10413607.

Morris, R.L., Graham, T.D.J., Kelvin, J., Ghisalberti, M., Swearer, S.E., 2019. Kelp beds as coastal protection: wave attenuation of ecklonia radiata in a shallow coastal bay. Ann. Botany 125, 235–246. http://dx.doi.org/10.1093/aob/mcz127, URL: https://academic.oup.com/aob/advance-article/doi/10.1093/aob/mcz127/5551380.

Mullarney, J.C., Henderson, S.M., 2010. Wave-forced motion of submerged single-stem vegetation. J. Geophys. Res. 115 (C12), C12061. http://dx.doi.org/10.1029/2010JC006448, URL: http://doi.wiley.com/10.1029/2010JC006448.

Ozeren, Y., Wren, D.G., Wu, W., 2014. Experimental investigation of wave attenuation through model and live vegetation. J. Waterw. Port Coast. Ocean Eng. 140 (5), 04014019. http://dx.doi.org/10.1061/(ASCE)WW.1943-5460.0000251, URL: http://ascelibrary.org/doi/10.1061/%28ASCE%29WW.1943-5460.0000251.

Peteiro, C., Freire, Ó., 2013. Biomass yield and morphological features of the seaweed saccharina latissima cultivated at two different sites in a coastal bay in the atlantic coast of Spain. J. Appl. Phycol. 25 (1), 205–213. http://dx.doi.org/10.1007/s10811-012-9854-9, URL: http://link.springer.com/10.1007/s10811-012-9854-9.

Plew, D.R., Stevens, C., Spigel, R., Hartstein, N., 2005. Hydrodynamic implications of large offshore mussel farms. IEEE J. Ocean. Eng. 30 (1), 95–108. http://dx.doi.org/10.1109/JOE.2004.841387, URL: http://ieeexplore.ieee.org/document/1435580/.

Riffe, K.C., Henderson, S.M., Mullarney, J.C., 2011. Wave dissipation by flexible vegetation. Geophys. Res. Lett. 38 (18), n/a. http://dx.doi.org/10.1029/2011GL048773, URL: http://doi.wiley.com/10.1029/2011GL048773.

Rosman, J.H., Denny, M.W., Zeller, R.B., Monismith, S.G., Koseff, J.R., 2013. Interaction of waves and currents with kelp forests (macrocystis pyrifera): Insights from a dynamically scaled laboratory model. Limnol. Oceanogr. 58 (3), 790–802. http://dx.doi.org/10.4319/lo.2013.58.3.0790, URL: http://doi.wiley.com/10.4319/lo.2013.58.3.0790.

Rosman, J.H., Koseff, J.R., Monismith, S.G., Grover, J., 2007. A field investigation into the effects of a kelp forest (macrocystis pyrifera) on coastal hydrodynamics and transport. J. Geophys. Res. Oceans 112 (2), 1–16. http://dx.doi.org/10.1029/2005JC003430, URL: https://agupubs.onlinelibrary.wiley.com/doi/pdf/10.1029/2005JC003430.

Sánchez-González, J.F., Sánchez-Rojas, V., Memos, C.D., 2011. Wave attenuation due to posidonia oceanica meadows. J. Hydraul. Res. 49 (4), 503–514. http://dx.doi.org/10.1080/00221686.2011.552464, URL: http://www.tandfonline.com/doi/abs/10.1080/00221686.2011.552464.

Sappati, P.K., Nayak, B., VanWalsum, G.P., Mulrey, O.T., 2019. Combined effects of seasonal variation and drying methods on the physicochemical properties and antioxidant activity of sugar kelp (saccharina latissima). J. Appl. Phycol. 31 (2), 1311–1332. http://dx.doi.org/10.1007/s10811-018-1596-x, URL: http://link.springer.com/10.1007/s10811-018-1596-x.

Sarpkaya, T., O'Keefe, J.L., 1996. Oscillating flow about two and three-dimensional bilge keels. J. Offshore Mech. Arct. Eng. 118 (1), 1–6. http://dx.doi.org/10.1115/1.2828796, URL: https://asmedigitalcollection.asme.org/offshoremechanics/article/118/1/1/434651/Oscillating-Flow-About-Two-and-ThreeDimensional.

Schneider, C.A., Rasband, W.S., Eliceiri, K.W., 2012. NIH Image to imagej: 25 years of image analysis. Nature Methods 9 (7), 671–675. http://dx.doi.org/10.1038/nmeth.2089, URL: http://www.nature.com/articles/nmeth.2089.

Stévant, P., Rebours, C., Chapman, A., 2017. Seaweed aquaculture in Norway: recent industrial developments and future perspectives. Aquac. Int. 25 (4), 1373–1390. http://dx.doi.org/10.1007/s10499-017-0120-7, URL: http://link.springer.com/10.1007/s10499-017-0120-7.

van Veelen, T.J., Fairchild, T.P., Reeve, D.E., Karunarathna, H., Van Veelen, T.J., Fairchild, T.P., Karunarathna, D.E., 2020. Experimental study on vegetation flexibility as control parameter for wave damping and velocity structure. Coast. Eng. 157, 103648. http://dx.doi.org/10.1016/j.coastaleng.2020.103648, URL: https://linkinghub.elsevier.com/retrieve/pii/S0378383919300663.

Vettori, D., Nikora, V., 2017. Morphological and mechanical properties of blades of saccharina latissima. Estuar. Coast. Shelf Sci. 196, 1–9. http://dx.doi.org/10.1016/j.ecss.2017.06.033.

Vettori, D., Nikora, V., 2018. Flow–seaweed interactions: a laboratory study using blade models. Environ. Fluid Mech. 18 (3), 611–636. http://dx.doi.org/10.1007/s10652-017-9556-6, URL: http://link.springer.com/10.1007/s10652-017-9556-6.

Vettori, D., Nikora, V., 2019. Flow-seaweed interactions of saccharina latissima at a blade scale: turbulence, drag force, and blade dynamics. Aquatic Sciences 81 (4), 61. http://dx.doi.org/10.1007/s00027-019-0656-x, URL: http://link.springer.com/10.1007/s00027-019-0656-x.

Vettori, D., Vettori student, D., Nikora Professor, V., Nikora, V., 2020. Hydrodynamic performance of vegetation surrogates in hydraulic studies: a comparative analysis of seaweed blades and their physical models. J. Hydraul. Res. 58 (2), 248–261. http://dx.doi.org/10.1080/00221686.2018.1562999, URL: https://www.tandfonline.com/doi/full/10.1080/00221686.2018.1562999.

Xiao, X., Agusti, S., Lin, F., Li, K., Pan, Y., Yu, Y., Zheng, Y., Wu, J., Duarte, C.M., 2017. Nutrient removal from chinese coastal waters by large-scale seaweed aquaculture. Sci. Rep. 7 (1), 46613. http://dx.doi.org/10.1038/srep46613, URL: http://www.nature.com/articles/srep46613.

Yin, Z., Wang, Y., Liu, Y., Zou, W., 2020. Wave attenuation by rigid emergent vegetation under combined wave and current flows. Ocean Eng. 213, 107632. http://dx.doi.org/10.1016/j.oceaneng.2020.107632, URL: https://linkinghub.elsevier.com/retrieve/pii/S0029801820306338.

Zeller, R.B., Weitzman, J.S., Abbett, M.E., Zarama, F.J., Fringer, O.B., Koseff, J.R., 2014. Improved parameterization of seagrass blade dynamics and wave attenuation based on numerical and laboratory experiments. Limnol. Oceanogr. 59 (1), 251–266. http://dx.doi.org/10.4319/lo.2014.59.1.0251, URL: http://doi.wiley.com/10.4319/lo.2014.59.1.0251.

Zhu, L., Huguenard, K., Fredriksson, D.W., Lei, J., 2021.Wave attenuation by flexible vegetation (and suspended kelp) with blade motion: Analytical solutions, Adv. Water Resour., in revision.

Zhu, L., Huguenard, K., Zou, Q.-p., Fredriksson, D.W., Xie, D., 2020a. Aquaculture farms as nature-based coastal protection: Random wave attenuation by suspended and submerged canopies. Coast. Eng. 160, 103737. http://dx.doi.org/10.1016/j.coastaleng.2020.103737, URL: https://linkinghub.elsevier.com/retrieve/pii/S0378383919303990.

Zhu, L., Zou, Q., 2017. THREE-Layer analytical SOLUTION FOR WAVE attenuation BY SUSPENDED and nonsUSpended vegetation CANOPY. Coast. Eng. Proc. 1 (35), 27. http://dx.doi.org/10.9753/icce.v35.waves.27, URL: https://icce-ojs-tamu.tdl.org/icce/index.php/icce/article/view/8239.

Zhu, L., Zou, Q.-p., Huguenard, K., Fredriksson, D.W., 2020b. Mechanisms for the asymmetric motion of submerged aquatic vegetation in waves: A consistent-mass cable model. J. Geophys. Res. Oceans 125 (2), 1–31. http://dx.doi.org/10.1029/2019JC015517, URL: https://onlinelibrary.wiley.com/doi/abs/10.1029/2019JC015517.

Zijlema, M., Stelling, G., Smit, P., 2011. SWASH: An operational public domain code for simulating wave fields and rapidly varied flows in coastal waters. Coast. Eng. 58 (10), 992–1012. http://dx.doi.org/10.1016/j.coastaleng.2011.05.015, URL: https://linkinghub.elsevier.com/retrieve/pii/S0378383911000974.